SANDIA REPORT

SAND2017-3953 Unclassified Unlimited Release, UUR Printed April 17, 2017

Open Stack Thermal Battery Tests

Kevin N. Long, Kyle Fenton, Christine C. Roberts, Dennis Wong, Anne M. Grillet, Alexander J. Headley, and David Ingersoll

Prepared by Sandia National Laboratories Albuquerque, New Mexico 87185 and Livermore, California 94550

Sandia National Laboratories is a multi-program laboratory managed and operated by Sandia Corporation, a wholly owned subsidiary of Lockheed Martin Corporation, for the U.S. Department of Energy's National Nuclear Security Administration under contract DE-AC04-94AL85000.



A STATE OF

Issued by Sandia National Laboratories, operated for the United States Department of Energy by Sandia Corporation.

NOTICE: This report was prepared as an account of work sponsored by an agency of the United States Government. Neither the United States Government, nor any agency thereof, nor any of their employees, nor any of their contractors, subcontractors, or their employees, make any warranty, express or implied, or assume any legal liability or responsibility for the accuracy, completeness, or usefulness of any information, apparatus, product, or process disclosed, or represent that its use would not infringe privately owned rights. Reference herein to any specific commercial product, process, or service by trade name, trademark, manufacturer, or otherwise, does not necessarily constitute or imply its endorsement, recommendation, or favoring by the United States Government, any agency thereof, or any of their contractors or subcontractors. The views and opinions expressed herein do not necessarily state or reflect those of the United States Government, any agency thereof, or any of their contractors.

Printed in the United States of America. This report has been reproduced directly from the best available copy.

Available to DOE and DOE contractors from

U.S. Department of Energy Office of Scientific and Technical Information P.O. Box 62 Oak Ridge, TN 37831

Telephone: (865) 576-8401 Facsimile: (865) 576-5728

E-Mail: reports@adonis.osti.gov
Online ordering: http://www.osti.gov/bridge

 $Available \ to \ the \ public \ from$

U.S. Department of Commerce National Technical Information Service 5285 Port Royal Rd Springfield, VA 22161

Telephone: (800) 553-6847 Facsimile: (703) 605-6900

E-Mail: orders@ntis.fedworld.gov

 $On line\ ordering: \ http://www.ntis.gov/help/ordermethods.asp?loc=7-4-0\#on line\ ordering: \ http://www.ntis.gov/help/ordermethods.asp?loc=7-4-0\#on line\ ordering: \ http://www.ntis.gov/help/ordermethods.asp?loc=7-4-0\#on line\ ordering: \ http://www.ntis.gov/help/ordermethods.asp?loc=7-4-0\#on line\ ordering: \ http://www.ntis.gov/help/ordermethods.asp?loc=7-4-0#on line\ ordering: \ http://www.ntis.gov/help/ordermethods.asp?loc=7-4-0#$



SAND2017-3953 Unclassified Unlimited Release, UUR Printed April 17, 2017

Open Stack Thermal Battery Tests

Kevin N. Long, Christine C. Roberts, Anne M. Grillet, and Alexander J. Headley Engineering Sciences Center Sandia National Laboratories, Albuquerque NM 87185-0840

> Kyle Fenton, Dennis Wong, and David Ingersoll Power Sources Technology Group Sandia National Laboratories, Albuquerque NM 87185-0840

Abstract

We present selected results from a series of Open Stack thermal battery tests performed in FY14 and FY15 and discuss our findings. These tests were meant to provide validation data for the comprehensive thermal battery simulation tools currently under development in Sierra/Aria under known conditions compared with as-manufactured batteries. We are able to satisfy this original objective in the present study for some test conditions. Measurements from each test include: nominal stack pressure (axial stress) vs. time in the cold state and during battery ignition, battery voltage vs. time against a prescribed current draw with periodic pulses, and images transverse to the battery axis from which cell displacements are computed. Six battery configurations were evaluated: 3, 5, and 10 cell stacks sandwiched between 4 layers of the materials used for axial thermal insulation, either Fiberfrax Board or MinK. In addition to the results from 3, 5, and 10 cell stacks with either in-line Fiberfrax Board or MinK insulation, a series of cell-free "control" tests were performed that show the inherent settling and stress relaxation based on the interaction between the insulation and heat pellets alone.

Before ignition, we observed that less than 5% of the originally applied stack stress relaxed during fixed displacements periods of up to 72 hours for either insulation type. The percent of stress relaxation was less than has been observed in recent work [6]. However, during battery activation, we found that batteries built with Fiberfrax Board insulation relaxed to within 10-20 psi of the residual

nominal stress for each of the 3, 5, and 10 cell configurations while the residual stress on activation from the MinK insulated batteries was directly related to the number of cells. These findings were consistent with the "control" tests, which involved configurations without electrochemical cells in which MinK stacks relaxed by less than 10% of the nominal stress during heat pellet ignition. In contrast, Fiberfrax stacks relaxed by approximately 75%. We attribute these findings to the very different compliances between the two insulation layers resulting from differences in material behavior and layer thicknesses.

In addition to validation data, the Open Stack tests allowed us to quantitatively investigate the effects of stack stress (axial pressure) on battery electrochemical performance. Under the mild conditions studied here (stationary batteries, room temperature, open circuit for 1.5 seconds followed by a constant current (density) draw at 56 mA cm⁻² with 83 mA cm⁻² current pulses), we found no correlation between battery internal resistance and residual nominal pressures of 10 to 150 psi long after battery activation for these current loads.

The report details the experimental methods and data analyses approaches. It summarizes the experimental findings and concludes with recommendations for future tests.

Acknowledgment

The authors would like to thank the Power Sources Technology Group in general and David Ingersoll's laboratory in particular for access to the needed facilities. We also thank Phil Reu (1512) and Mike Bejarano (1535) for assisting us with the setup of the high speed camera equipment. Anthony Tanbukuchi (1535) provided an in-house python code package for analysis of the high speed camera CINE files, the native binary file format from high speed Phantom cameras that we used. We are very appreciative of the thorough review from Scott Roberts (1512) and Hans Papenguth (2547) which improved the clarity of the findings.

Contents

1	Introduction	11
2	Experiments	13
	Battery Materials and Stack Building Process	13
	Open Stack Test Setup, Execution and Data Collection	16
3	Data Analysis	21
	Battery Electrochemical Performance Analysis	21
	Cell Displacements	22
4	Results Summary Across All Batteries Tested	29
	Control Test Results Summary	29
	Stack Force Summary	30
	Electrochemical Performance Summary	35
	Cell Displacement Summary	37
5	Conclusions	43
	Key Findings	43
	Future Test Recommendations	44
Re	eferences	45

List of Figures

2.1	3 Cell Stack Layups for MinK and FF Insulated Batteries	15
2.2	Images of the Experimental Setup	17
2.3	Experimental Setup Schematic and Triggering	18
2.4	Test Matrix Completion Status	19
3.1	Extracting Electronic Resistance From the Voltage Signal	22
3.2	Intensity Decomposition of the Open Stack Images	25
3.3	Before and After 10 Cell MinK Stack	26
3.4	Initial and Final FFT Demonstration on a 3 Cell FF Test	27
4.1	Stack Force Comparison Control Tests with MinK and Fiberfrax Board Insulation .	32
4.1 4.2	Stack Force Comparison Control Tests with MinK and Fiberfrax Board Insulation . Stack Force Comparison for 3, 5, and 10 Cell Stacks with MinK and Fiberfrax Board Insulation	32
	Stack Force Comparison for 3, 5, and 10 Cell Stacks with MinK and Fiberfrax	
4.2	Stack Force Comparison for 3, 5, and 10 Cell Stacks with MinK and Fiberfrax Board Insulation	33
4.2	Stack Force Comparison for 3, 5, and 10 Cell Stacks with MinK and Fiberfrax Board Insulation	33 34
4.2 4.3 4.4	Stack Force Comparison for 3, 5, and 10 Cell Stacks with MinK and Fiberfrax Board Insulation	33 34 36
4.2 4.3 4.4 4.5	Stack Force Comparison for 3, 5, and 10 Cell Stacks with MinK and Fiberfrax Board Insulation	33 34 36 39

List of Tables

2.1	Electrochemical Cell Pellet Die Dimensions and Source Information	14
2.2	Insulation and Current Collector Dimensions and Source Information	14

Chapter 1

Introduction

High fidelity thermal battery performance models require extensive validation under known and relevant boundary conditions. We previously studied the use of transmission X-ray and subsequent Moiré analysis of the battery stack from as-manufactured thermal batteries and showed that internal displacements could be determined in conjunction with measurements of battery electrochemical behavior [4]. The key advantage to the X-ray tests were that they represented as-manufactured boundary conditions. This same feature was their key disadvantage. Batteries are expensive, and customization must be done during assembly, which is costly. These constraints make the X-ray approach impractical for the purposes of generating a diverse suite of validation data meant to harden the fidelity of our predictive tools over a range of boundary conditions associated with a variety of batteries and environments. We needed another approach to acquire validation data.

To this end, we developed the Open Stack test platform in 2014. For this technique, tests are performed in two stages: assembly and preloading occur in a normal dry room environment while battery activation and measurements occur in a glove box in an Argon environment. In the first stage, battery stacks are assembled under normal dry room conditions, preloaded, and allowed to relax in the test fixture. They are then transported in a sealed can and introduced into the Argon environment. When a test battery is ignited, force, displacement, and electrochemical measurements are simultaneously measured and controlled. This test platform, which is described extensively in section 2, allows for much more rapid exploration of how manufacturing and environmental conditions affect a battery's performance than was possible in the X-ray Moiré work. We are specifically interested in measuring how the battery stack layout (pellet dimensions, number of cells, and the number/thickness of insulation layers at the top and base of the stack), applied stack pressure during manufacture, and residual stack pressure after battery activation affect a battery's electrochemical performance under controlled current loads. Apart from full battery assembly tests, these experiments were unique for their constant strain design in 2014. The Power Sources Group has since adopted the fixture designed in this experiment for other studies.

The role of mechanical stress during and after activation on the thermal battery electrochemical performance has not been thoroughly explored. During activation, the separator pellet compacts as the electrolyte melts. This deformation is taken up by the insulation as it elastically unloads. If the combined thickness of axial insulation is too small relative to the total separator thickness, then the stack will fully relax to near zero residual stress. Under the opposite extreme (too much insulation compared to the separator), then very little of the stack stress will unload. We will observe these behaviors from this test series and the negligible impacts they have on electrochemical measure-

ments performed here. These findings are some of the first to assess the role of mechanical stress on electrochemical performance.

The remainder of the report is organized into four sections: Section 2 discusses the Open Stack experimental setup, section 3 presents data analysis procedures associated with the battery discharge data and displacement analysis, and section 4 summarizes results from the suite of tests. Finally, we provide conclusions from this study and recommendations for future tests in section 5.

Chapter 2

Experiments

We tested 3, 5, and 10 electrochemical cell arrangements sandwiched between 4 layers of MinK and Fiberfrax Board insulation. The sides of the stack were exposed to an argon environment in a glovebox. Each stack was preloaded to approximately 200 psi of nominal stress. This corresponded to a 500 lbf closing force, which was the limit of our Omega pancake load cell. The closing force was applied using an Instron uniaxial load frame. Once the 500 lbf closing force was reached and verified with both the Instron and Omega load cells, stopping screws were used to maintain that pressure. The screws were tightened in sequence to attempt to evenly distribute the load. The load cell readout was recorded over time prior to battery ignition so that the load relaxation could be monitored. Typical pre-test relaxation times were between 1 hour and 1 day. The battery stack was then ignited from the side with a single strip of heat paper along the length of the stack that was held in place with Kapton tape. Ignition was achieved by resistively heating a wire that was in direct contact with the heat paper. As the battery activated, the relaxation of the load was recorded, the outside of the stack was imaged with a high speed camera to analyze the surface motion, and 1.5 seconds after the ignition signal, a prescribed current draw was applied while the voltage was measured. In the following sections, details of the battery builds, experimental apparatus, test protocol, and data analysis are presented.

Battery Materials and Stack Building Process

The electrochemical cells were composed of a stainless steel current collector, Fe / KClO₄ heat pellet, Li(Si) anode, LiCL-KCl / MgO separator, and FeS₂ cathode. These pellets were generated inhouse. Individual pellet dimensions and source Request for Action (RFA) and Specific Use Specification (SS) numbers are summarized in Table 2.1. Grafoil was not used in any of the battery configurations. The Open Stack battery design and materials were guided by the MC3815 and MC3816 battery designs.

Each battery stack was sandwiched by two layers of insulation and two additional heat pellets at the top and bottom. MinK and Fiberfrax Board (FF) insulation specimens punched to the appropriate diameter were used in these tests. Details of the insulation materials are summarized in Table 2.2. Both the Fiberfrax and MinK discs were punched out of as-received and as-purchased (respectively) sheets of material using a large punch. Insulation was heat treated at 600 C for four hours prior to stacking. No insulation, glass tape, or can was present to support/insulate the

Table 2.1. Electrochemical cell pellet die dimensions and source information. For all cases except the collectors, the density tolerance was listed as \pm 0.1 g cm⁻³, and the thickness tolerance was listed at 0.08 mm.

Material	Diameter (mm)	Thickness (mm)	Pressed Density (g cm ⁻³)	RFA / SS Numbers for Powder or Reagents
Heat Pellet (86/14 (UD) M)	44.5008	0.4414	3.35	14-08-004 / SS297149-000
Cathode (XFLC176J)	43.8734	0.2728	2.91	14-08-007 / SS379481-201
Separator (EB 17)	44.3027	0.2883	1.80	14-08-005 / SS370633-200
Anode (44% LiSi)	43.8734	0.3638	1.00	14-08-006 / SS370711-200

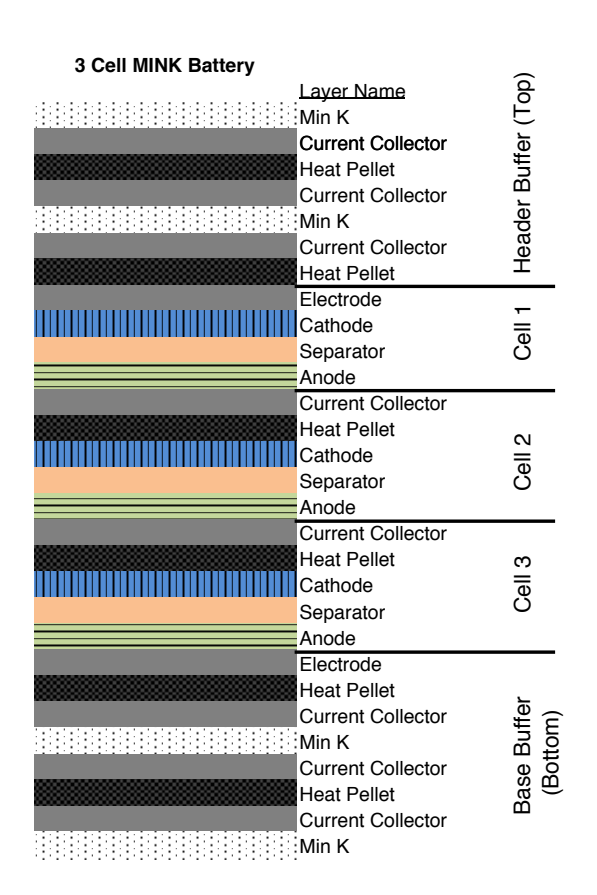
perimeter of the batteries, which was intentionally left open for viewing.

Detailed stack layout for the 3 cell MinK and FF stacks are provided schematically in Figure 2.1. The 5 and 10 cell batteries included more electrochemical cells while the "Control Tests" used similar layouts but without electrochemical cells. Note that for all the tests, four layers of insulation were used, regardless of the number of electrochemical cells. Thus, the net thicknesses of MinK and FF were 25 and 5.1 mm, respectively, for each stack. Additionally, the MinK layers were always separated from the heat pellets with current collectors while FF layers were in direct contact with them. The four extra current collectors in the MinK batteries and the additional mass of MinK changed the thermal mass noticeably between the corresponding batteries (MinK and FF assemblies).

Table 2.2. Insulation layer and current collector dimensions and source information.

Insulation Layer	Diameter (mm)	Thickness (mm)	Density (g cm ⁻³)	Source
Stainless Steel Collector	41.3-47.6	0.072- 0.254	8.0	Not Applicable
MinK	44.45	6.25	0.333	Measurement
Fiberfrax Board	44.45	1.27	0.745	Measurement

The 86/14 heat pellets were rated to produce 260 calories per gram of material when ignited. With the geometry and density for the pellets and insulation layers from tables 2.1 and 2.2, the heat balance, which is defined here as the total calorific output per gram mass of a single cell, for each



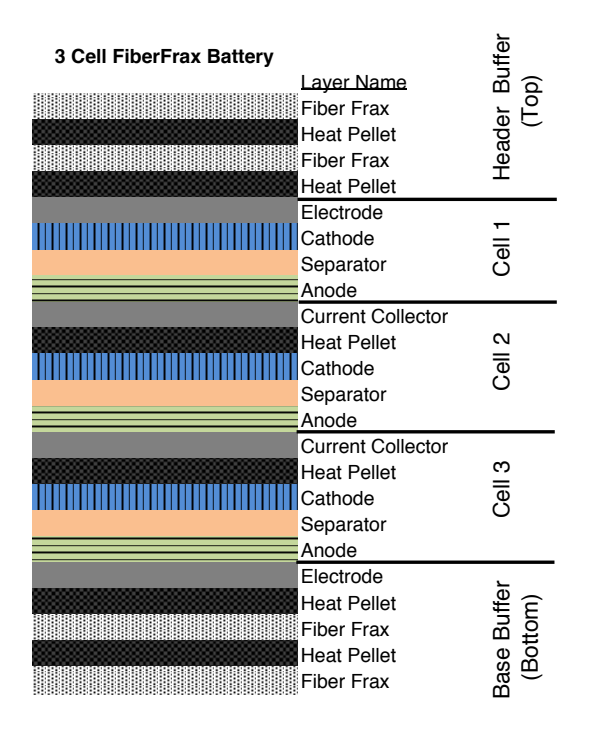


Figure 2.1. 3 Cell Stack Layouts for MinK and FF Insulated Batteries. The 5 and 10 cell batteries and "Control" stacks involve similar layups. Note the current collectors between MinK and the heat pellets that do not exist in the FF Battery.

battery is straightforward to calculate. The heat balance varied because the current collectors used for the tests increased in massmid test suite. Hence, the heat balances ranged from 43.5 calories per gram for the 3 mil collectors to 39.5 calories / gram for the 5 mil collectors. These heat balances are summarized at the end of this section in Figure 2.4, which also shows the status of each test outcome.

The battery stack was assembled in the fixture using two axial guide posts to align the individual pellets. We acknowledged that the side of the battery farthest from these guides involves some geometric mismatch since the pellets were not exactly the same diameter. The build included two discs of insulation at the top and bottom along with two additional heat pellets at the top and bottom for all assemblies (see Figure 2.1). A thick steel disc capped the top insulation layer and acted both as a load spreader and thermal mass to protect the 500 lbf rated pancake load cell (PN, manufacuter, location) placed above it. The stack assembly was encased between two steel compression plates used to maintain the preloaded stress on the battery stack. These plates were connected with four threaded posts with bolts (positioning stops) above and below them. After the stack was assembled and aligned within the fixture, the plates were compressed to the 500 lbf load

limit of the load cell, which is approximately 210 psi for nominally 1.75-inch diameter cells in Table 2.1. The loading process was achieved by incrementally tightening the stopping bolts, one at a time to keep the compression plates parallel and took approximately 5 minutes. Once the target load was reached, the bolts were no longer adjusted. Changes in the axial force were monitored and recorded over 4-72 hours.

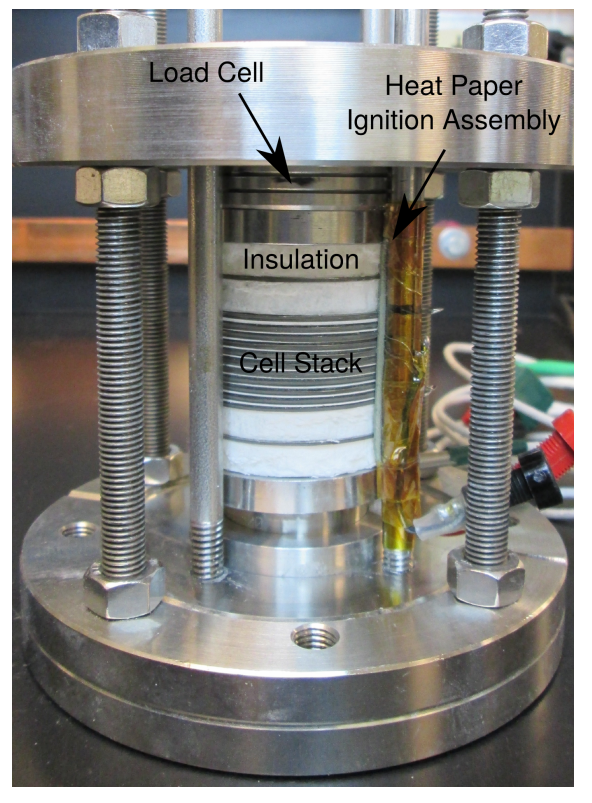
Stack assembly and preloading occurred within a dry room with a maximum dewpoint of -40C to ensure the stability of all the materials involved. Stress relaxation was recorded within the dry room until test time. Then the fixture was sealed in a metal can and transported to the purge chamber for transport into the argon glovebox.

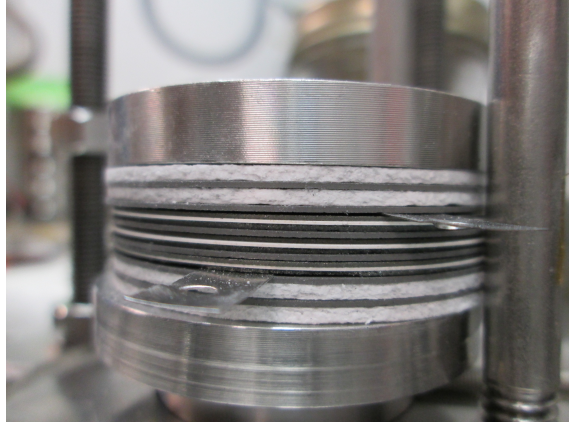
Open Stack Test Setup, Execution and Data Collection

Once inside the glovebox, the test assembly was completed as shown in Figure 2.2. The battery stack was further instrumented with the ignition assembly, which consisted of a strip of heat paper affixed to the battery with Kapton tape. A circuit was connected to the electrical leads (electrodes in Figures 2.1 and 2.2) placed at the top/bottom of the electrochemical stack connected to the Maccor 4200 Battery Tester for current/voltage control. The load cell wiring was reconnected to an NI multi-function Data Acquisition (DAQ) system. Outside the glove box, a Phantom V9 camera with a K2 lens using a CF4 high magnification adapter was focussed onto the stack surface such that the entire length of the stack was within the field of view. Occasionally, not all the heat pellets in the stack ignited from the heat paper during battery activation. Midway through the test series, a second strip of heat paper was added to the battery opposite the ignition strip to ignite heat pellets that may not have ignited initially. While rise time measurements were discarded in these cases, the activated battery electrochemical responses were useful.

To provide higher fidelity validation data, the Open Stack setup included a common trigger for all measurement systems. That is, the trigger signal sent to ignite the heat paper also activated the phantom camera, load cell DAQ, and initiated the Maccor current voltage/current measurements. This gave us a common time zero, which we define as the moment that the trigger pulse was activated. The trigger process was controlled within a LabView environment as depicted in Figure 2.3(b). The Maccor battery tester did not operate precisely on the common time zero because its rate of data acquisition was comparatively low (20 Hz) as compared to the phantom camera and load cell (500 Hz or more). The zero time for the Maccor measurements relative to the ignition time was estimated, as will be discussed later in the report. However, given the electrochemical measurement objectives for this study, the estimation of the Maccor zero time was inconsequential.

During battery ignition, the load relaxation was recorded and high speed images were taken at a rate of 500 frames per second for the first 5 seconds and 10 frames per second for the remainder of the test to capture the long term deformation. During the first 1.5 seconds after the trigger signal, the battery's open circuit voltage was measured. Our objective was to avoid drawing current during the rise time. After 1.5 seconds, we switched to current control. Here, we drew a nominal current of 0.8 A (52.6 mA cm⁻²). Every 15 seconds, we pulsed the current draw to 1.25 A (82.2





(a) 10 Cell Test with MinK Discs

(b) 3 Cell Test with FF Discs

Figure 2.2. Images of the Open Stack experimental setup

mA cm⁻² for 1 second). Our objective was to monitor how the ohmic, ionic, and total resistances changed with each current pulse as well as to determine when the battery would freeze out. Because these batteries lacked insulation/glass tape around the perimeter, the thermal and mechanical environments were quite different than in typical assembled batteries.

Our test plan called for a complete set of 3, 5, and 10 cell Open Stack battery tests with both MinK and Fiberfrax Board insulation in triplicate (18 tests total). Unfortunately, many tests were either complete or partial failures. Many of the complete failures involved thermal runaway. Most of these runaways occurred because the current collectors initially used were too small in diameter compared with surrounding pellets (41.3 vs. 44+ mm). As a result, a portion of the heat pellet interfaced the anode directly (though initially separated by the collector thickness). When the heat pellets were ignited, the heat transfer from the heat pellet to the anode across this open space was sufficient to excessively heat and melt the anode which led to runaway. This issue was corrected later with larger diameter collectors. With the exception of one additional runaway, batteries in all other tests performed as intended. Most tests were partial failures in which some measurement system did not perform correctly, or the pellets did not all ignite when the initial heat paper strip burned. In these partial failure cases, typically some set of measurements were still successfully performed. A summary of each test is provided in Figure 2.4.

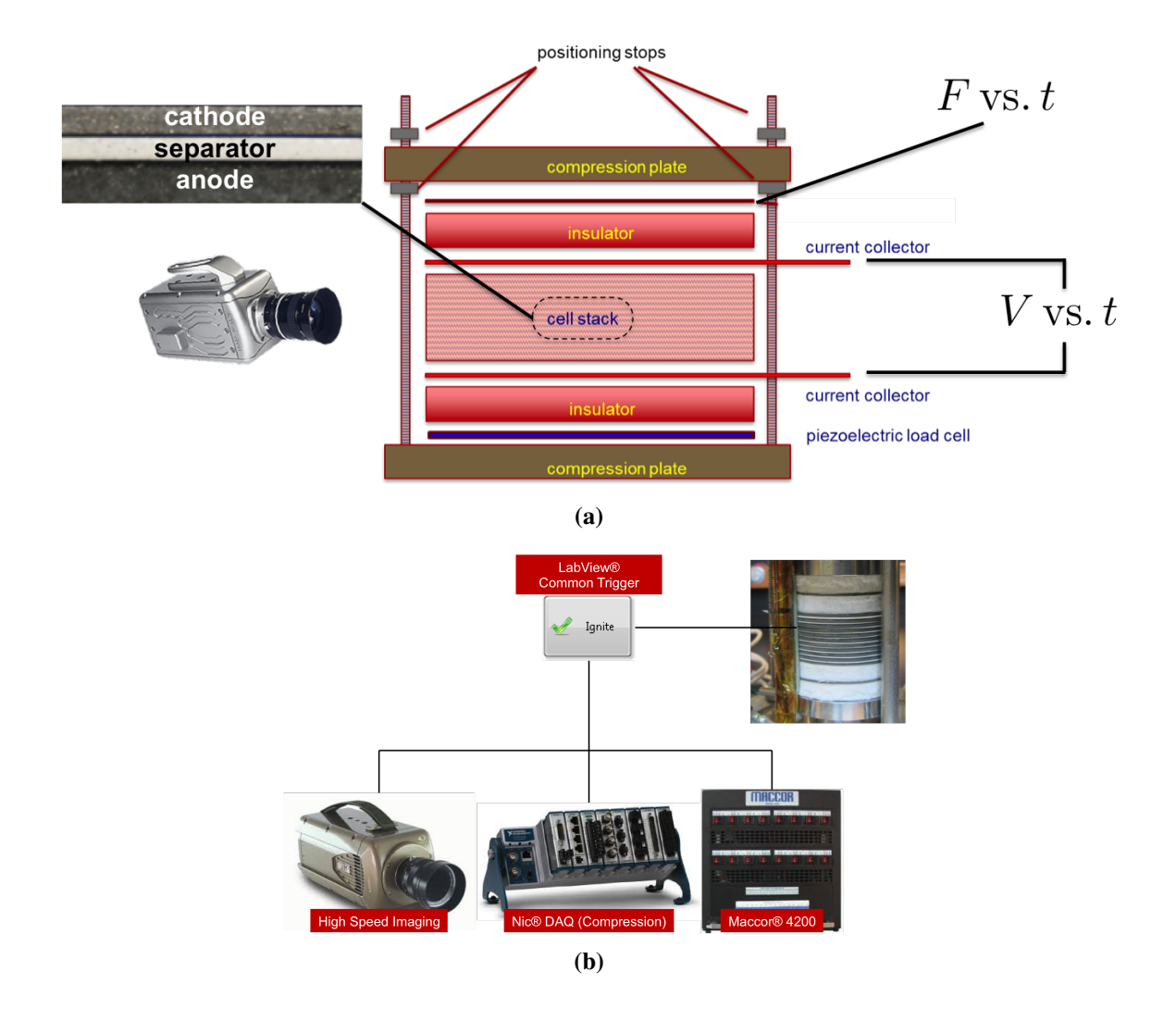


Figure 2.3. Experimental setup schematic (a) and triggering scheme (b).

For completeness, we note that temperature measurements were performed early in the test cycle to prove that the load cell was sufficiently protected within the fixture from large temperature changes. Temperature increases as high as 15 °C were recorded in the vicinity of the load cell, which was well within the load cell's normal operation range. No other temperature measurements were performed. Future tests could involve strategically placed thermocouples or surface measurements from an infrared camera in conjunctions with the high speed camera outside the glove box.

Finally, we distinguish between the Control and Open Stack tests. Control stacks followed similar build, preload, transport, and firing protocols. Here, the electrochemical stack was omitted along with the associated measurements. Additionally, high speed images were not taken for every control test, and no displacement analyses were performed.

		Heat Pellet Calorific	Current Collector
T ID.	NOTES	Output / Mass Per Cell	(Number-Thickness
Test ID	NOTES:	, , , , ,	(mil), Diameter (inches)
9_9_3Cell_FF_3	Anode Decomposition (heat pellet contact)	43.5	
9_9_3Cell_FF_4	Anode Decomposition (heat pellet contact)	43.5	
9_9_3Cell_MinK_2	Insulation Burned	43.5	1 - 3 , 1.626
9_9_72H_Control_FF_3		CONTROL	6 - 3 , 1.626
9_4_72H_Control_FF_4		CONTROL	6 - 3 , 1.626
9_11_3Cell_FF_3	Anode Decomposition (heat pellet contact)	43.5	1 - 3 , 1.626
9_11_3Cell_MinK_2	Anode Decomposition (heat pellet contact)	43.5	1 - 3 ,1.626
9_11_3Cell_MinK_4		43.5	1 - 3 , 1.626
9_12_3Cell_MinK_3		41.4	1 - 4 , 1.75
9_12_3Cell_MinK_4		37	1 - 10 ,1.875
9_4_72H_Control_MinK_1		CONTROL	1 - 10 ,1.875
9_4_72H_Control_MinK_2		CONTROL	1 - 10 ,1.875
9_15_3Cell_FF_3	Misfire - Unlit Pellets	37	1 - 10 ,1.875
9_15_3Cell_FF_4	Video Capture Error		1 - 4 , 1.75
9_16_5Cell_FF_1	Lost Positive battery lead		1 - 4 , 1.75
9_16_5Cell_MinK_2	One non-lit pellet	41.4	1 - 4 , 1.75
9_16_5Cell_MinK_3	Video Capture Error	41.4	1 - 4 , 1.75
9_17_5Cell_FF_3	Anode Decomposition (heat pellet contacted anode)	41.4	1 - 4 , 1.75
9_17_10Cell_MinK_2	No Video. Cine file lost during post processing	41.4	1 - 4 , 1.75
9_17_10Cell_MinK_4	Misfire - Unlit Pellets	41.4	1 - 4 , 1.75
9_18_3Cell_FF_4	No voltage/current during the rise time. Maccor manually triggered	41.4	1 - 4 , 1.75
9_18_3Cell_MinK_1	No voltage/current during the rise time. Maccor manually triggered	41.4	1 - 4 , 1.75
9_18_5Cell_FF_2	Load cell data corrupted	41.4	1 - 4 , 1.75
9_18_10Cell_FF_3	Not all the pellets burned after ignition. Backup heat paper ignited	41.4	1 - 4 , 1.75

Figure 2.4. Test matrix completion status and heat balance. Red indicates that the test failed such that partial data could not be recovered. Yellow indicates that part of the data collection of test outcome involved errors but much of the remaining data was available. Green indicates the test completed as planned. The "Test ID" column provides details on the date (m_dd), pre-ignition relaxation time (Hours), Number of Cells (3, 5, or 10 Cell), and insulation type (MinK or FF). If the pre-ignition relaxation (in hours) is not indicated, batteries were packaged, transported to the glove box, and tested as soon as possible.

Chapter 3

Data Analysis

Battery Electrochemical Performance Analysis

With regard to electrochemical performance, our objective was to determine each battery's resistance response over time associated with the current pulses. Following the 1.5 second open circuit voltage measurement, 0.8 A nominal and 1.25 A pulse current draws were applied (1 second pulses every 16 seconds). The measured voltage immediately dropped (ohmic) at the start of each current pulse. To a lesser extent, the voltage continued to drop over time (non-ohmic) until the applied current draw returned to its nominal state. This initial voltage drop divided by the change in current is a measure of the electronic (ohmic) resistance in the battery. A similar resistance measure is extracted at the end of the current pulse as it jumps back down to the nominal current draw. We label these two resistances $R_{0.i}$ and $R_{0.f}$ as they are associated with the electronic (ohmic) resistances at the start (initial—i) and end (final—f) of the current pulse. They are calculated trivially from Ohm's law. For example, the initial electronic resistance is $R_{0.i} = \Delta V_{0.i}/\Delta I$. A reasonable review of these techniques is found in reference [7].

During the current pulse, the voltage continued to drop over time. This continued voltage decrease was the result of several simultaneous processes all with different time scales. Ionic diffusion of the molten electrolyte [7], solid state diffusion of Lithium in the anode, and reaction kinetics at the electrode particle surfaces [1] all could contribute to a change in the measured resistance over time. Moreover, these mechanisms are all highly temperature dependent and may change even during a 1 second pulse given the lack of radial insulation on the batteries. Since we did not control the temperature, we will not pursue analysis of these data (during the current pulse). An example of how we extract these resistances as well as what a typical voltage history looks like during a current pulse is shown in Figure 3.1.

The voltages before and after the pulse are not the same. The voltage always diminishes over time for both the nominal and pulse current draw states. We dismiss the possibility that we are observing a change in chemistry as the battery state of charge transitions from the first to the second plateau. We would see this phenomenon as an offset in the nominal voltage curve, and we do not observe such a drop until the batteries freeze out [2] within 3 to 8 minutes of the ignition signal. Therefore, we conjecture that the change in voltage over time from the start to the end of each current pulse is related to a slow temperature drop within the battery and the associated increase in transport resistance and reduction in chemical kinetics.

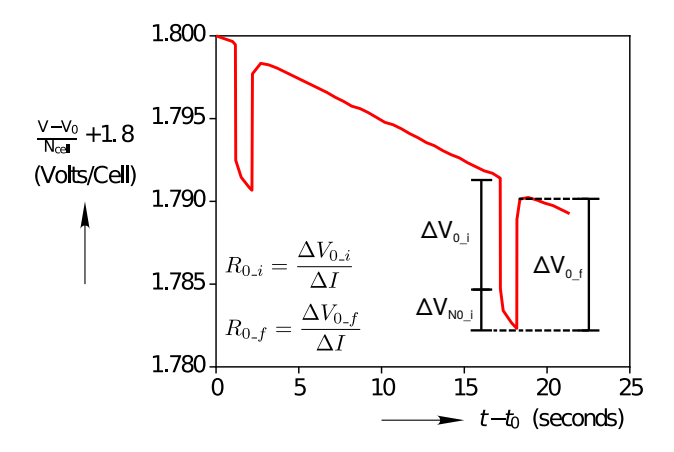


Figure 3.1. Extracting electronic resistance from the voltage signal. Here, the basis for determining the initial $(R_{0.i})$ and final $(R_{0.f})$ electronic resistances associated with the step up and then step down in applied current is shown. The time dependent voltage change, $V_{N0.i}$, represents the combination of other effects: ionic resistance, capacitance discharge, temperature dependence of the reaction kinetics, solid state diffusion in the electrodes, and possibly more. Turning the non-ohmic voltage change into a resistance cannot use the same definition (Ohm's law) since it is not associated with a current change, but rather it could be associated with the current draw during the pulse.

Cell Displacements

The objective of this analysis was to extract the displacement field on the transverse surface of the open battery stack during ignition and operation. A sequence of images captured from the Phantom camera setup as described in Section 2 for each battery was analyzed. We pursue two analysis techniques: 1) a modified form of edge tracking (which we label "Peak") and 2), a discrete Fast Fourier Transform analysis of the image intensity as a function of axial position in the stack (which we label "FFT"). The first method is conceptually similar to edge tracking but is sufficiently different that we describe it in detail here. Essentially, the method tracks the intensity centroids of the different pellets within the stack. As these centroids move relative to each other, we are able to back out relative displacements and strains. The raw images are 8-bit grayscale, and the high reflectivity regions correspond to the separator pellets in each cell. At the finest resolution, our approach furnishes inter-cell relative displacements. However, we can also determine the average deformation per cell over the whole stack. The specific analysis procedure is as follows:

- 1. Crop and rotate the first (time zero) image such that only the electrochemical cells are visible and they are oriented with a common vertical axis.
- 2. Rescale the pixel intensity of the image within the cropped region to be between 0 and 1.

- 3. Divide the cropped, rotated, and normalized image into $N \ge 1$ regions from left-to-right. For each region, average the normalized intensity across each row. Identify the center of the highest average intensity layers along the vertical axis in each region, which marks a unique location in this region of the battery.
- 4. Using inputs from Step 1 as fixed, repeat Steps 1-3 for each subsequent image in time. The locations of high intensity peaks in each region can now be compared at different points in time, and the displacement (in integer units of pixels) can be extracted.
- 5. Return the positions of each high intensity peak in each region for each frame.

To compute the strain within a cell or between multiple cells, we take the original distance between intensity peaks (number of pixels) as L_0 just prior to battery activation, and with each image, we compute the current number of pixels separating these intensity peaks, which we label L(t). Then, we compute the axial engineering strain in the usual way, $\varepsilon(t) = \frac{L(t) - L_0}{L_0}$.

Steps 2 and 3 are illustrated in Figure 3.2 wherein one can see that the intensity can vary substantially from region to region but that the separator layers can generally be extracted from the images. For comparison, this 10 cell MinK battery is compared before and after to show the extent of deformation and change in the images in Figure 3.3.

In previous Open Stack tests, both a wide angle and a zoomed camera were used, and edge tracking proved effective for computing the displacements [4]. Here, with much less resolution from the wide angle only images, we did not attempt edge tracking and instead followed the procedure above, which is essentially a row-averaged edge tracking capability. This method is more tolerant when dealing with smoke than direct edge tracking, but it provided noisier results than desired.

Because of the difficulties in handling intensity peaks coming in and out of view, we also pursued the FFT approach. For this analysis, the image intensity per pixel location of the cropped and rotated images was averaged across the entire width of the stack at each timestamp. These data were then processed using an FFT function to obtain the stack averaged frequency data at each time. The guiding principle here is that after the zero frequency amplitude (the mean intensity of the image) the returned frequency peaks should correspond to the number of peaks (around 3, 5, and 10 separators depending on the number of cells) over the total pixel length and the associated harmonics. As the stack compresses and the separators move closer together, the frequency of the peaks returned from the FFT analysis will increase slightly as the spacing between peaks decreases. This increased frequency is demonstrated in Figure 3.4. The inverse of the peak frequency (i.e., the average number of pixels between peaks) can then be used to calculate the strain of the stack by using the value at time zero as a reference. By tracking the change in the returned frequency over the course of the test, strain values can be associated with each time step. The following image shows the initial and final FFT results associated with a 3 cell FF stack as an example. Note that zero-padding (adding a string of zeros to the signal array) and a Hanning window function were used to increase the frequency resolution and reduce the associated ringing for the analysis, respectively.

The FFT analysis method is less sensitive to the pixilation noise that plagues the Peak analysis technique, and suffers less from data gaps as the FFT will return a result at each timestamp. However, image quality and artifacts (e.g., flame propagation, smoke, etc.) can still affect the result of the analysis, so some noise and error is still to be expected. Furthermore, the FFT analysis does not provide any information regarding displacements between individual cells (e.g., cell 1 to cell 2) as the FFT is applied over the entire stack. This method is continuing to be developed for future tests.

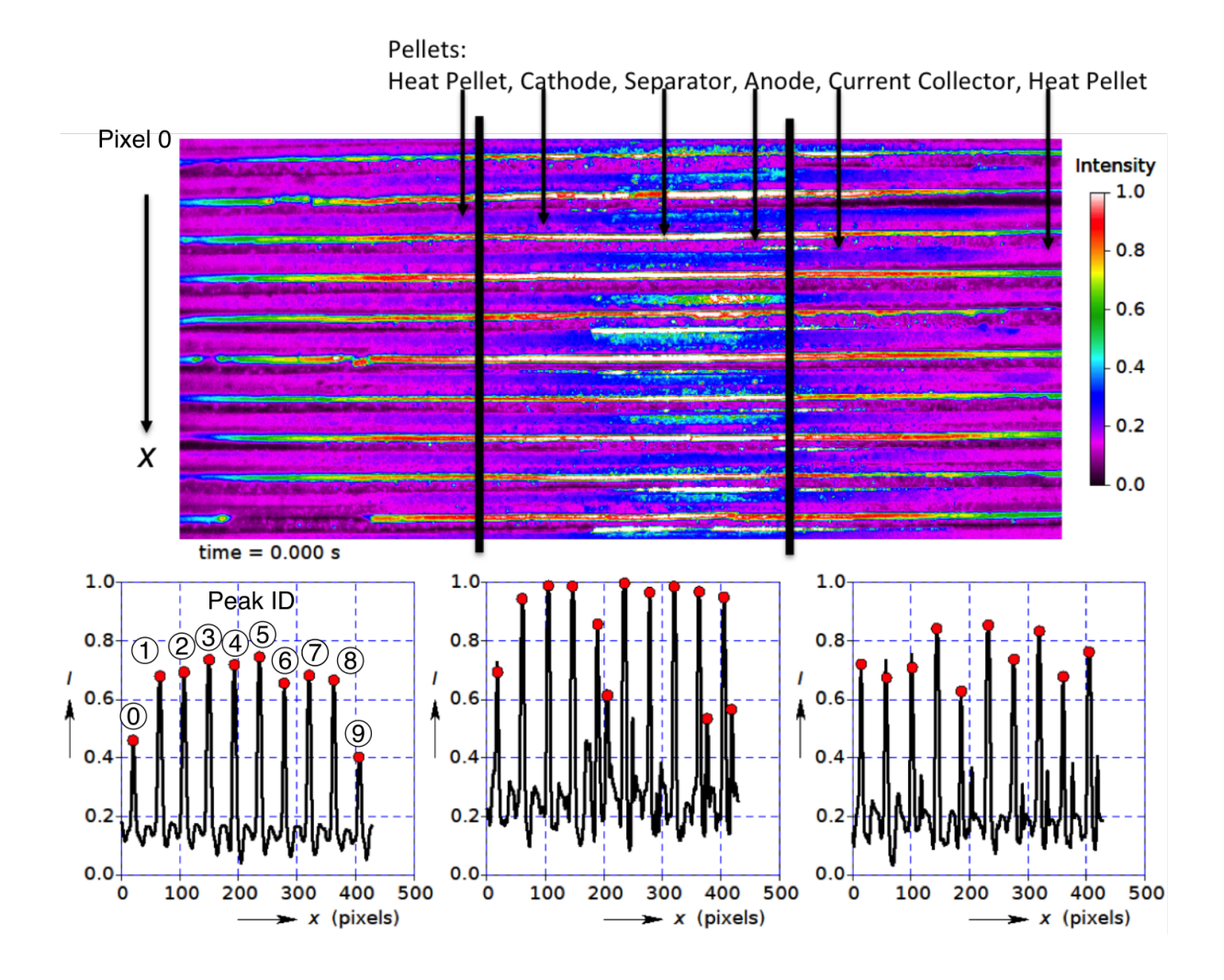
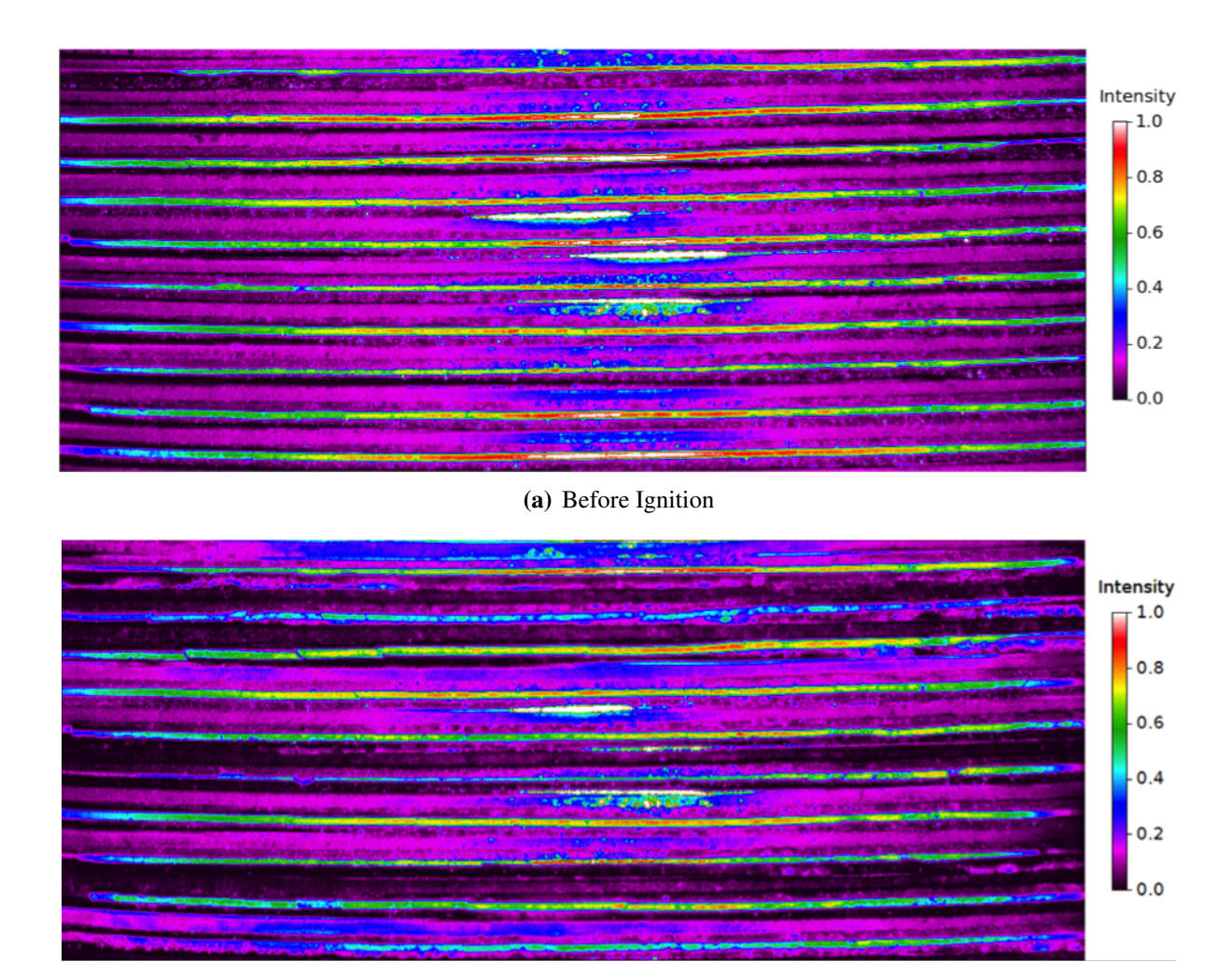


Figure 3.2. Intensity decomposition of the open stack images. Left, center, and right region-averaged intensity decomposition of the battery stack images across a 10 cell Open Stack are shown. A false color map has been applied to the grayscale images to distinguish the different layers within the stack. The averaged intensities corresponding to each region have been normalized by the peak intensity throughout the entire battery for this snapshot in time and are shown (rotated 90 degrees) in the lower three figures corresponding to the left, center, and right regions. The high reflectivity is evident in the center region compared with the left and right regions.

Red circles indicate the midpoints of the intensity peaks and correspond approximately to separator pellets. These peaks are labeled starting from zero closest to the zero pixel location. 3, 5, and 10 cell batteries have 3 (0-2), 5 (0-4), and 10 (0-9) peaks respectively. An example of this numbering is shown in the left-side averaged intensity in the lower left figure. The relative motion of these intensity peak over time is used to determine inter-cell relative strains across different locations in the battery. For example, 0-4 refers to the strain between peaks 0 and 4.



(b) Near Freeze Out

Figure 3.3. Before and after snapshots of the stack surface for a 10 cell MinK stack. Note the change in peak intensity "finger prints". The distribution and even number of peaks can change during the battery lifetime, which can cause the loss of specific peaks during analysis.

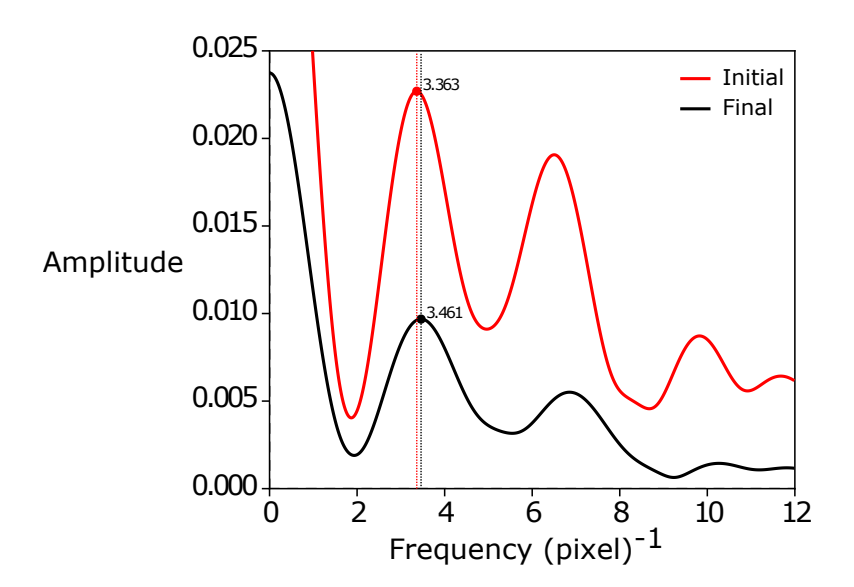


Figure 3.4. Initial and final FFT demonstration on a 3 cell FF test. FFT analysis of the initial and final images from a 3 cell Fiberfrax test shows a shift in the frequency with cell compaction. The unit of the frequencies listed is peaks per the entire pixel range of the image (here 240 pixels). The inverse of this frequency, which is the average number of pixels between peaks, is used for the strain calculation.

Chapter 4

Results Summary Across All Batteries Tested

Control Test Results Summary

Beginning with the Control Tests, we provide both the short and long time stack stress responses during and after battery activation in Figure 4.1. Focusing on the short time scale—including battery rise and several seconds after—in Figure 4.1(a), we see that the two MinK insulation tests show negligible stress relaxation (approximately 5%) on heat pellet activation. Furthermore, the stress states are nearly the same between the 4 hour and 72 hour preloads on the MinK Control Tests as well as after ignition. The stress relaxes only for the first second for the MinK Control Tests, and then little is observed afterwards.

By comparison, the Fiberfrax Board Control Tests show that the Fiberfrax control stacks relax significantly more than the MinK control stacks prior to heat pellet ignition. The stress in the stack for the 72 hour aged FF batteries is approximately 10% lower than its corresponding 4 hour aged counterpart whereas MinK showed a much smaller difference between the 4 hour and 72 hour aged cases. Just after heat pellet ignition, substantial stress relaxation occurred. Focusing on the early time data, Figure 4.1(a), the stress relaxed by 60% to 80% of the starting value for the Fiberfrax Board Control Tests. The Fiberfrax material is stiffer than MinK and the FF discs were thinner; as such, the FF discs are much stiffer than the MinK discs such that less internal deformation is required to relax the stress state.

Still, these Control Tests suggest that much of the preload in Fiberfrax Board Insulated batteries is independent on the electrochemical stack. Compared with the MinK, the starting stress states varied more, which may be due to variations in loading these stiffer pellets within the Open Stack fixture. Also, it is interesting to note that during the Fiberfrax Board Control Tests the stress appears to recover after long periods of time. At this point, we conjecture that the Fiberfrax Board pellets themselves heat up and expand causing more compressive stress to develop. This phenomenon was not observed in the MinK insulation which shows steady behavior out to several minutes.

Stack Force Summary

We discuss the Open Stack force measurements with characteristic stack nominal stress data vs. time for each battery and insulation type. For all batteries, the initial rapid stress relaxation associated with separator pellet melting, crush, and insulation relaxation occurs within one second of the heat paper ignition signal. We refer to this first second as the mechanical rise time, which is likely longer than the rise time measurement associated with the open circuit voltage. As with the Control Tests in Section 4, there is a big difference between the MinK and Fiberfrax Board insulated batteries in terms of residual stack stress after activation. The three Fiberfrax Board cases relax to nearly the same stress in the activated state (between 10 psi and 20 psi or 90% to 95% stress relaxation from the pre-ignition state) as shown in Figure 4.2(a). The Fiberfrax Board insulated batteries relaxed more than in the associated Control Tests and to nearly the same stress state for the 3, 5, and 10 cell configurations. For the conditions tested, these findings corroborate the "rule of thumb" that the residual stack stress in Fiberfrax Board insulated batteries relaxes to around 10 psi after activation [3, 8].

In contrast, the MinK battery relaxation post rise time depended on the number of cells and therefore on the relative thickness between the insulation and separator pellets, which are primarily responsible for axial deformation in the battery stack [5]. Stress relaxations of approximately 20%, 40%, and 60 % relative to the pre-ignition stress occurred during the rise time for the 3, 5, and 10 cell MinK stacks, respectively (Figure 4.2(b)). The measured stack stress vs. time is plotted for the remaining life of the batteries in Figure 4.2(c). As with the control tests in Figure 4.1(c), the Fiberfrax insulated batteries show non-intuitive recovery behavior, which is most likely caused by warpage (potato-chipping) of the stainless steel collectors during the test. This causes the overall stack to expand slightly and push against the load cell. To a lesser extent, a stress recovery is also observed in the MinK batteries likely for the same reason, but because the compliance of the MinK discs is much higher, the deformation causes less of a change in the stack stress as compared to the FF discs.

We attempt to comprehend the difference between the Fiberfrax Board and MinK insulation batteries by plotting the stack stress after battery rise against the thickness ratio defined in Equation 4.1 and 4.2:

$$t_{1}^{*} = \frac{N_{\text{cells}}t_{\text{cell}} + t_{\text{HP in insulation}}}{t_{\text{insulation}}},$$

$$t_{2}^{*} = \frac{N_{\text{cells}}t_{\text{separator}}}{t_{\text{insulation}}},$$

$$(4.1)$$

wherein the number of cells, thickness per cell, and total heat pellet thickness within the insulation are divided by the total insulation thickness. The purpose of the first normalization is to incorporate the control tests into the battery tests since stress relaxation (especially for the FF cases) was significant. The second normalization is the more natural method based on the expectation that the majority of compaction during activation is from the separator.

The stress after the rise time (1.25 seconds after ignition) is plotted against these normalized

thicknesses in Figure 4.3 for a representative datum from each battery and Control Test. Note that the current collector thicknesses are ignored in the cell thicknesses calculation. Because the Control Tests showed significant relaxation for the Fiberfrax Board cases, we include the thickness normalization in Equation 4.1, which slightly distinguishes the Fiberfrax Board cases from the MinK Control Tests as seen in Figure 4.3(b). The second normalized thickness, Equation 4.2, is motivated by the assertion that the deformation that causes the insulation layers to unload chiefly arises from the separator pellets within the battery stack. This normalization does not distinguish the control tests.

With either thickness normalization scheme, the residual stress after battery activation rapidly diminishes by ratios of 1 to 2 (see Equations 4.1 and 4.2). The limiting cases are reasonable. In the limit of zero non-dimensional thickness, there is too much insulation, and it cannot elastically unload during battery activation while in the case of little insulation, the battery unloads very quickly. These findings may be particularly important for shock and vibration analysis of batteries in terms of preserving a minimum preload. However, as we will find later in the report, the residual stack stress does not correlate to the electronic internal resistance measurements.

The Fiberfrax and MinK insulation results are different in Figure 4.3. Consistently, the Fiberfrax Board insulation cases involve larger non-dimensional thicknesses, which we expect to deliver smaller residual stack stresses in the active state. However, the normalization is imperfect. Future efforts may consider instead a net stiffness (modulus * Area / thickness) normalization, which could properly account for the fact that the Fiberfrax insulation is both thinner and of higher compressive modulus and hence should be inherently stiffer than MinK considered here.

We summarize key points from the results in this section:

- 1. Battery activation involves an interplay between compaction of the separator and elastic unloading of the insulation discs to accommodate this deformation.
- 2. Key to preserving stack stress after activation is that the compliance is sufficiently large in the insulation layers and the initial closing force (initial stack stress) is sufficiently high.
- 3. All FF batteries investigated in this report had compliances too low to preserve appreciate stack stress after activation with the exception (approximately) of the 3 cell battery. Without changing the design, the initial stack stress must be significantly higher, or the design could be altered to add more FF layers.
- 4. MinK batteries in this report had sufficient compliance to accommodate the different cell numbers (and therefore net compaction strains), but from Figure 4.3(b), there will be a number of cells (approximately 18 for this configuration of MinK discs) in which the residual stack stress will fall to zero.

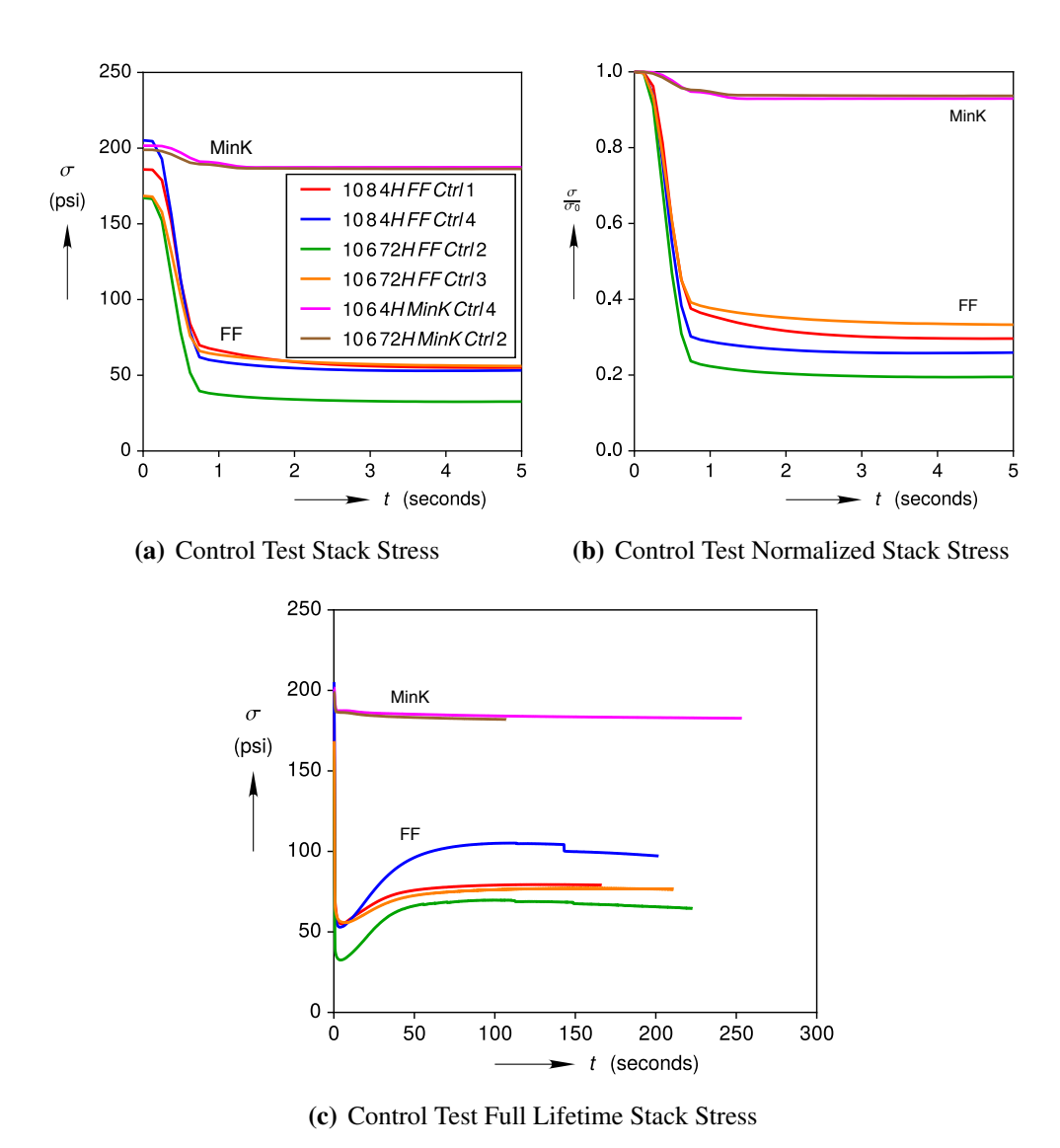


Figure 4.1. Stack Force Comparison Control Tests with MinK and Fiberfrax Board Insulation. The stack force comparisons during and immediately after the rise time (a) and for the first several minutes (c) until the control stacks cooled from the "control" tests are shown. In (b), the stack force is normalized by its initial value just prior to ignition. For each stack, four layers of insulation were used with a heat pellet between each layer, and the length of hold time in advance of heat pellet activation is provided in the legend.

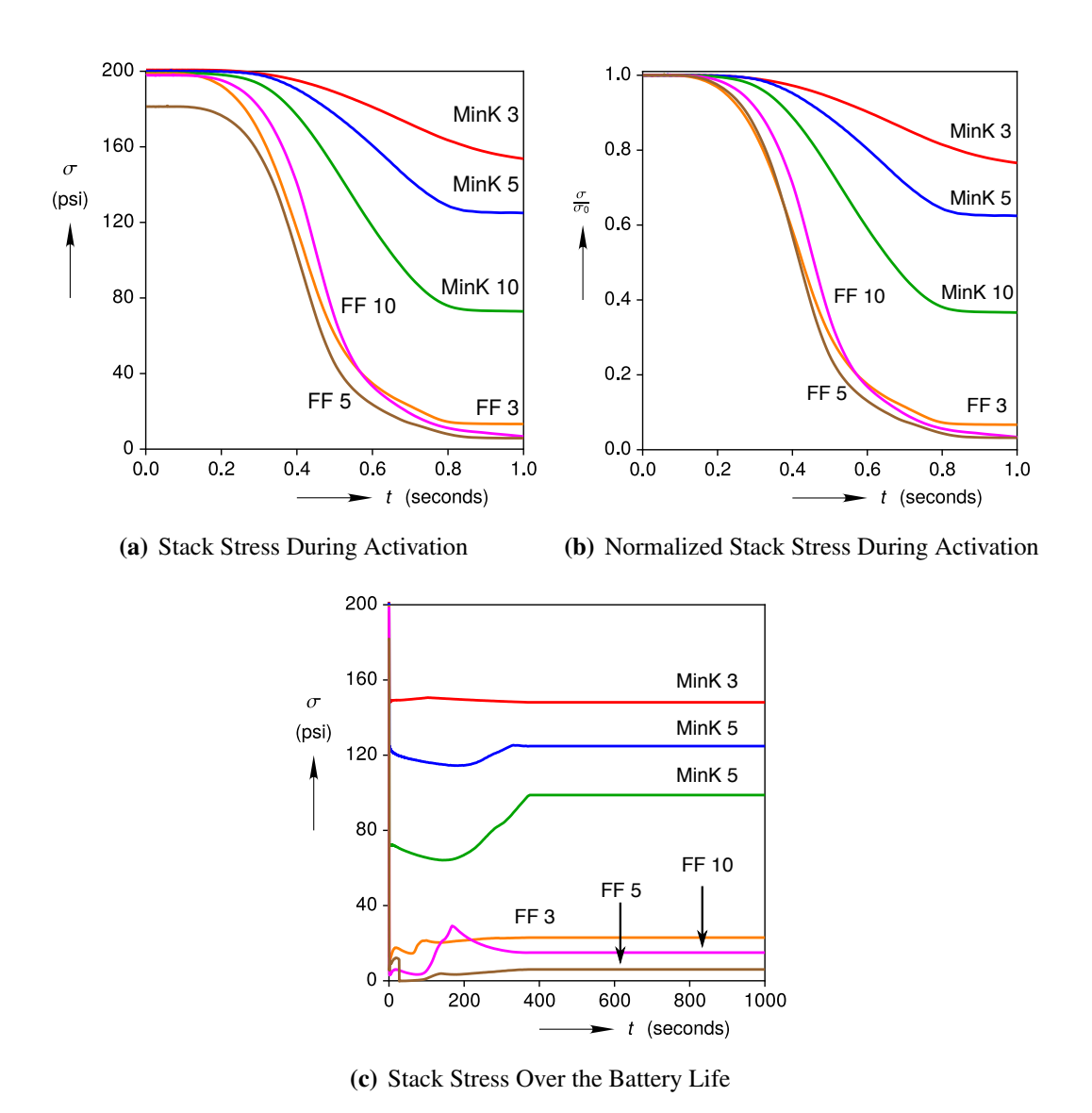
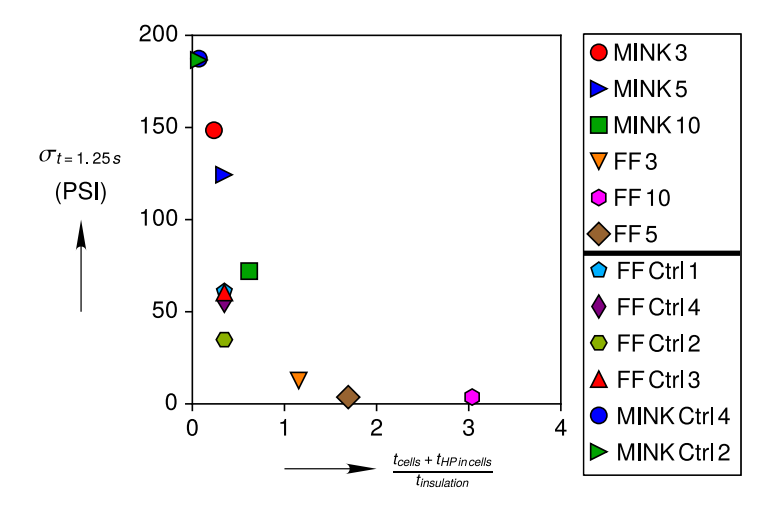
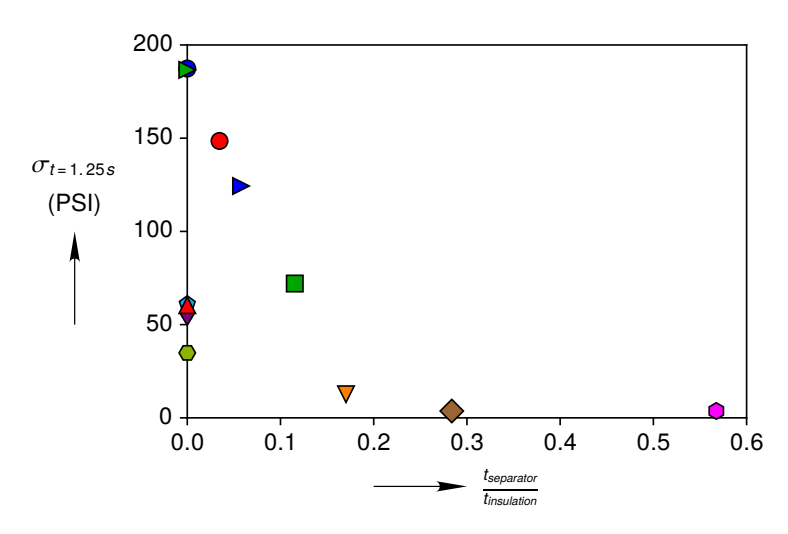


Figure 4.2. Stack Force Comparison for 3, 5, and 10 Cell Stacks with MinK and Fiberfrax Board Insulation. The rise time response is shown in (a) and normalized by the initial stress in (b). The full lifetime stress response is shown in (c). The increase in force after approximately 1 minute is associated with warpage of the stainless steel collectors.



(a) Residual Stack Stress After Rise: Method 1



(b) Residual Stack Stress After Rise: Method 2

Figure 4.3. Residual stress during activation vs. normalized thicknesses. The remaining axial stress 1.25 seconds after the trigger signal (activation) for the 3, 5, 10, and Control stacks using MinK and Fiberfrax Board insulation layers is shown. (a) Gives the stress at 1.25 seconds for each experiment with a normalized thickness that includes the total thickness of the cells + heat pellets in the header/footer divided by the total thickness of insulation while (b) gives the total thickness of the separator pellets divided by the total insulation thickness. In the latter case, control experiments have no separator thickness. Therefore in (b), they register at zero on x-axis. The cell thicknesses do not include the current collector.

Electrochemical Performance Summary

We present selected electrochemical results from each battery type and insulation case, and we will show that the data herein support the assertion that the electronic resistances at the start and end of the applied current pulses are not significantly affected by different residual stack stress conditions between 10 and 150 psi in the activated battery state of the battery. The open circuit voltage response was collected for the first 1.5 seconds. Afterwards, batteries were subjected to pulsed current control conditions. A typical applied current history and corresponding voltage measurement starting 1.5 seconds following the ignition signal are shown in Figure 4.4(a) and 4.4(b) respectively. From the latter plot, one may quickly estimate the freeze out time as the onset of when the battery voltage under nominal current draw drops precipitously. The 3 cell Fiberfrax and MinK insulation cases froze out in a similar amount of time (around 100 seconds). However, the battery types differed with more cells. The 5 and 10 cell Fiberfrax Board insulation batteries froze out after 180 and 300 seconds, respectively, in contrast to the 5 and 10 cell MinK batteries, which froze out after 280 and 340 seconds.

Because the exterior surface-to-volume ratio of these (constant diameter cylindrical) stacks is invariant to the stack height, we would expect to see no difference in the 3, 5, and 10 cell stacks freeze out times due to convection or the total heat source changes from the three different cases. Since they have different freeze out times, the end effects (heat conduction through the insulation) must be important. As one increases the number of electrochemical cells, a limit should be reached in which the ratio of convective area along the sides of the battery is much greater than the conductive area through the insulation layers at the top and bottom. In this limit, we expect the batteries to freeze out in similar amounts of time regardless of insulation type. We do not observe this limit even for the 10 cell batteries here, though the difference in freeze out times for the different insulations does decrease going from 5 to 10 cells (100 to 40 seconds).

We next focus on the first 20 seconds of battery voltage responses for each battery case in Figure 4.4(c). The voltages are normalized by the number of cells. The voltage datum is set to 1.8 Volts to mimic single cell data, and 3, 5, and 10 cell voltage data are normalized to this datum. We choose this short time scale to show the battery performance well before any batteries froze out. We see that with the exception of the 3 cell MinK and Fiberfrax Board insulation batteries, the voltage responses per unit cell, are nearly the same in this short time limit. Since the 3 cell batteries froze out earlier, we expect temperature effects to cause these batteries to see larger voltage swings than the other batteries that remained active longer.

Following the method discussed in Section 3 and Figure 3.1, we computed the battery electronic resistance at the beginning and end of each current pulse. Although the resistance at the pulse end is always larger than that at the start of the pulse, the trends between batteries are the same, so we show only the electronic resistance measurements at the pulse end in Figure 3.1. Here, the freeze out time is evident as the sudden increase in resistance, which is only seen at this time window for the two 3 cell batteries. Otherwise, we see no ordering of the resistance behaviors associated with residual stack stress. This fact is especially evident for the 3, 5, and 10 cell MinK batteries with activated stresses of 160 psi, 120 psi, and 80 psi each. Their resistances are comparable to those of Fiberfrax Board batteries with residual stresses less than 20 psi.

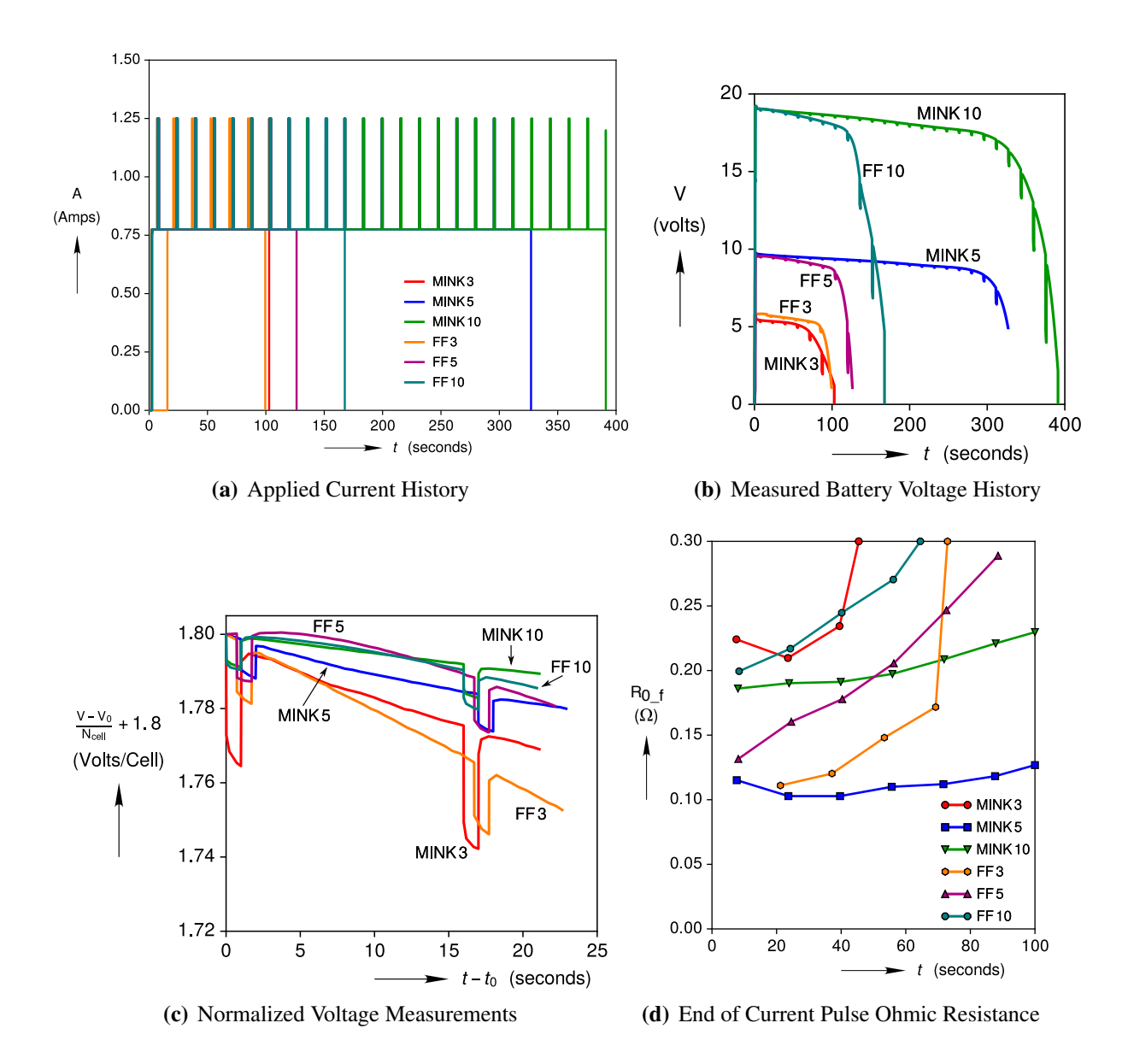


Figure 4.4. Discharge and resistance data. The applied current density (a), measured voltage response (b) normalized to the number of electrochemical cells in the stack are shown. (c) Voltage drops around the first and second pulses. The time and voltages have been adjusted so the different cases would begin from the same location. (d) Ohmic (electronic) resistance at the end of the current pulse vs. time. See Figure 3.1 for a definition of this resistance. FF and MinK insulations are indicated in the legend followed by the number of electrochemical cells used in each test.

Cell Displacement Summary

We will show in this section the characteristic strains experienced in the 3, 5, and 10 cell battery stacks with the two insulation configurations. Analysis was not performed on Control Tests because high speed imaging was not always available for those tests. We begin with the simplest picture of strain in the battery: the strain across all cells in the battery referenced to the undeformed cold state image and averaged across the battery diameter. This analysis provides the net average strain in each cell, but it does not account for variations along the diameter, nor does it give details of where the strain is localized within a given cell. The rise time and full lifetime average cell strain results for selected 3, 5, and 10 cell FF Board and MinK batteries are presented in Figure 4.5. Both the Peak (solid lines) and FFT (dashed lines) analysis methods are presented for comparison purposes.

The Peak and FFT methods are in good agreement in Figure 4.5(a) and 4.5(b) for the FF batteries, but agreement is comparatively poor for the MinK battery configurations. For FF, the Peak lacks data for the full life 3 cell configuration, but otherwise, the two methods are in both quantitative agreement, which serves as a validation that each method produces reasonable results.

For the MinK configurations, during rise time, only the 3 and 10 cell configurations are qualitatively similar with an error larger than the Peak noise threshold between the 10 cell analyses. The analysis methods do not agree with the 5 cell configuration during the rise time. We note that the FFT analyses of the 3, 5, and 10 cell configuration strains are consistent with the stress relaxation trend for these same configurations in Figure 4.2. Therefore, we are more inclined to trust the FFT results. During the battery lifetime, the Peak and FFT methods produce similar behaviors for the 5 and 3 cell batteries. However, after about 50-100 seconds, the Peak method shows a decrease in deformation compared with the continued increasing deformation determined from the FFT method. There are no full life 10 cell MinK battery data. Hence, those curves are missing in Figure 4.5(d).

For the Min-K batteries, typical activated battery average cell strains are 10%, 5%, and 3% for the 3, 5, and 10 cell configurations respectively. For the FF configurations, the typical activated average strains are closer and not clearly correlated with the number of cells (about 3-5% for any of the 3, 5, and 10 cell configurations). These observations are consistent with the residual stresses after activation for the MinK and FF batteries configurations in Figure 4.2. The MinK batteries show different residual stress and deformation from the activation process while the FF battery configurations show little variation. The deformation, however, is not uniform within the batteries. As will be seen shortly, more deformation is seen near the ignition heat paper strip than on the far side indicating that we may expect non-trivial deformation variations across other side-fired batteries, although they are typically ignited with 3 points rather than 1. Even center-fired batteries may slump more in the middle than the outer boundary [4].

For the remaining displacement analyses, only the Peak method is used to look at how the deformation changes across the battery diameter. We begin with the strain analysis of typical 3 cell Fiberfrax Board and MinK insulation batteries (the 9_9_3Cell_FF and 9_18_3Cell_MinK cases) for which the camera images were divided into three equal regions as shown in Figure 3.2. The row-averaged axial strain history (measured between the top and bottom intensity peaks) is plotted for

the three regions in Figure 4.6. The top and bottom rows show the left-center-right region averaged strains along the battery axis for the Fiberfrax Board and MinK insulated batteries, respectively. A set of two strains is plotted for each battery, which corresponds to relative motions between the center (1)-to-top (0) intensity peaks and the center (1)-to-bottom (2) intensity peaks. The behavior is quite different for the left images. Here, we see that the center-to-bottom strain (red 1-2) is tensile for the Fiberfrax case (Figure 4.6(a)) while the center-to-top strain (black 0-1) is compressive and slowly increases over time from 3 to 5 or 8% strain. The MinK left figure result, Figure 4.6(a), shows the 1-0 and 1-2 strains having the same behavior at first (10% compressive strain), but then the two differ over the battery life.

The apparent tensile behavior is either associated with current collector potato chipping or with deficiencies in our algorithm to track "unique" intensity peaks. Because the batteries compress overall, it is possible for other high intensity regions to come into the field of view and be picked up by the analysis routine. We conjecture that the red 1-2 curves likely are affected by this scenario and should not be considered.

It is clear that the data in Figure 4.6 and all subsequent displacement/strain analysis figures are noisy. The source of this noise is pixelation. We resolve few pixels across each cell with the wide angle view. The number of pixels per cell varies based on the zoom required to image the stack and insulation. For the 10 Cell MinK stack in Figures 3.2 and 3.3, there are approximately 35 pixels per cell, which places a minimum on the error of +/- 3%. We are seeing much larger errors in the displacement measurements which further suggests an issue with the algorithm.

As we move to the center of the battery (Figures 4.6(b) and 4.6(d) for FF and MinK), we cannot track the bottom strain (Red 1-2) for FF, and we can only see it for the first 80 seconds of the MinK battery. This center region fluctuates less than the left region with strains stabilizing to 5 and 15% strain, respectively. Interestingly, it takes most of the activated life to realize the final strains in contrast to the short time duration of the stress relaxation of previous sections. Moving on to the right hand side near the heat paper, strains are the largest for the FF 3 cell battery at approximately 10% in compression for both FF and MinK. The strain values are comparatively stable in time. The higher strains near the first location of heat pellet activation are consistent with previous studies.

Moving on to the 5 cell stacks, we consider the 9_18_5Cell_FF_2 and 9_16_5Cell_MinK_2 batteries. Again, we measure from near the center of the battery axis (2) and compute strains across intensity peaks upward (1-0) and downward (3-4). These data are richer than the 3 cell data. Now, MinK regions left, center, and right all show a range of strains at a particular time. The ordering of these strains is not monotonic, such as center-to-outward or top to bottom. We are still working on explaining this finding. Also, while more deformation is seen near the heat paper (right), these data fluctuate more than the center and left images.

Finally, we move on to the 10 cell stacks and examine the 9_18_10Cell_FF and 9_17_10Cell_MinK. Generally, these show similar behavior as before. For Fiberfrax batteries, strains from the middle to the bottom appear to be near a net zero while strains from the middle of the axis to the top are compressive around 7% strain. For the MinK, a complete set of high speed images was not taken, and therefore, only the rise time data is available. Over this short duration, we see strains of 2-4% in compression reached with an anomolous curve showing tensile behavior.

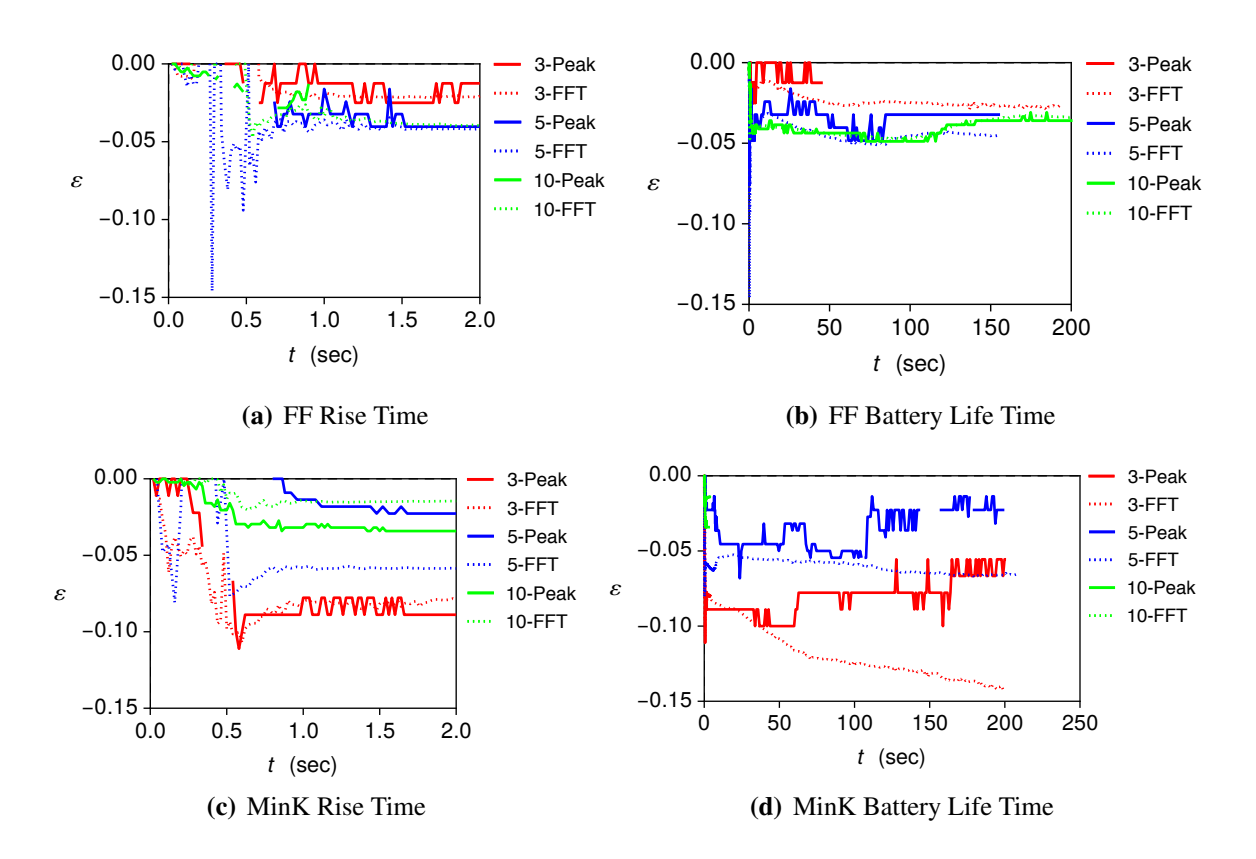


Figure 4.5. Average cell strains. The net strains averaged across the diameter for each battery configuration are shown for both the Peak (solid) and FFT (dashed) analysis methods. The MinK 5-cell battery images were not captured after the rise time, and hence, there are no data for this configuration in Figure 4.5(d). Because of smoke and other complications, frequently one cannot resolve intensity peaks throughout the entire tests, which leads to gaps in the strain for the Peak method. The FFT method does not suffer from this issue.

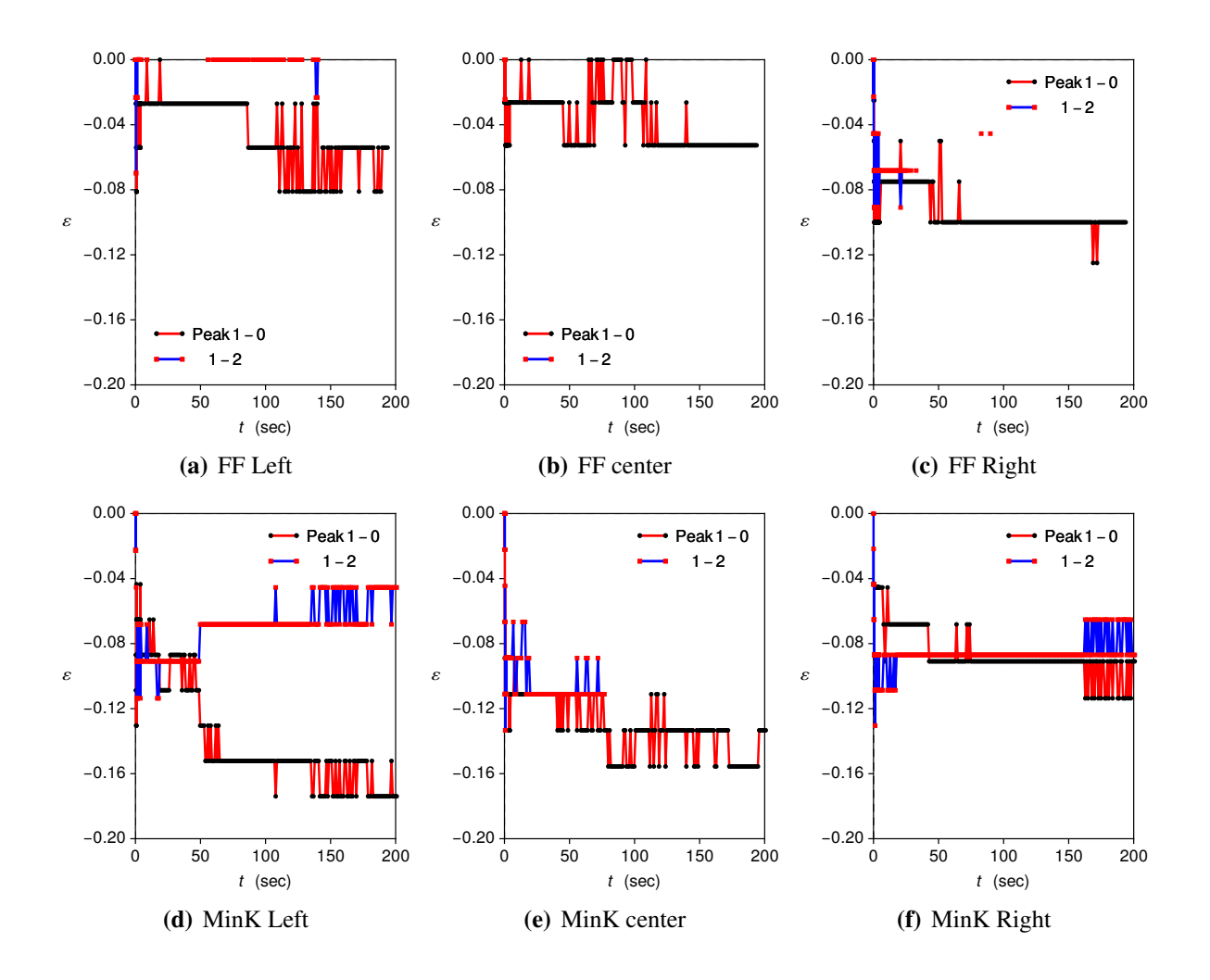


Figure 4.6. 3 cell stack strains. Strains in 3 Cell Fiberfrax Board and MinK insulated batteries averaged in the left, center, and right image regions are shown measured across peak image intensity regions as discussed in Figure 3.2. Because of smoke and other complications, frequently one cannot resolve intensity peaks throughout the entire tests. This loss of data is evident for the "1-2" peaks in both the FF and MinK center region plots. Characteristic strains are 3-10 % in compression for FF and 10-15 % for MinK 3 cell batteries with the largest strains occurring in the right regions next to the heat pellet.

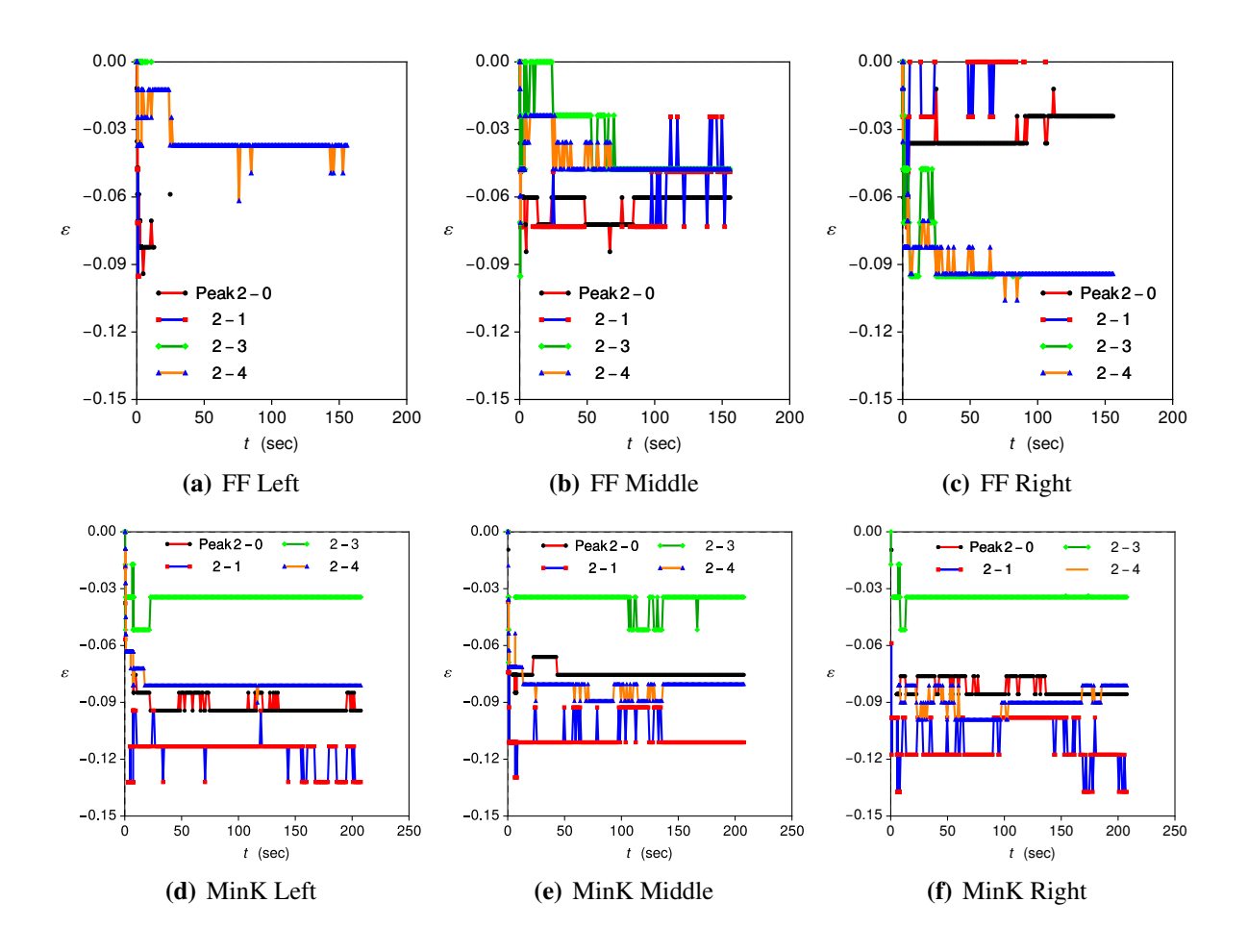


Figure 4.7. 5 cell stack strains. Strains in 5 Cell Fiberfrax Board and MinK insulated batteries averaged in the left, middle, and right image regions are shown measured across peak image intensity regions as discussed in Figure 3.2. Because of smoke and other complications, frequently one cannot resolve intensity peaks throughout the entire tests. This loss of data is evident for the "FF Left" data. Characteristic strains are 4-6 % in compression for FF and around 10-12 % for MinK 3 cell batteries with the largest strains occurring in the right regions next to the heat paper.

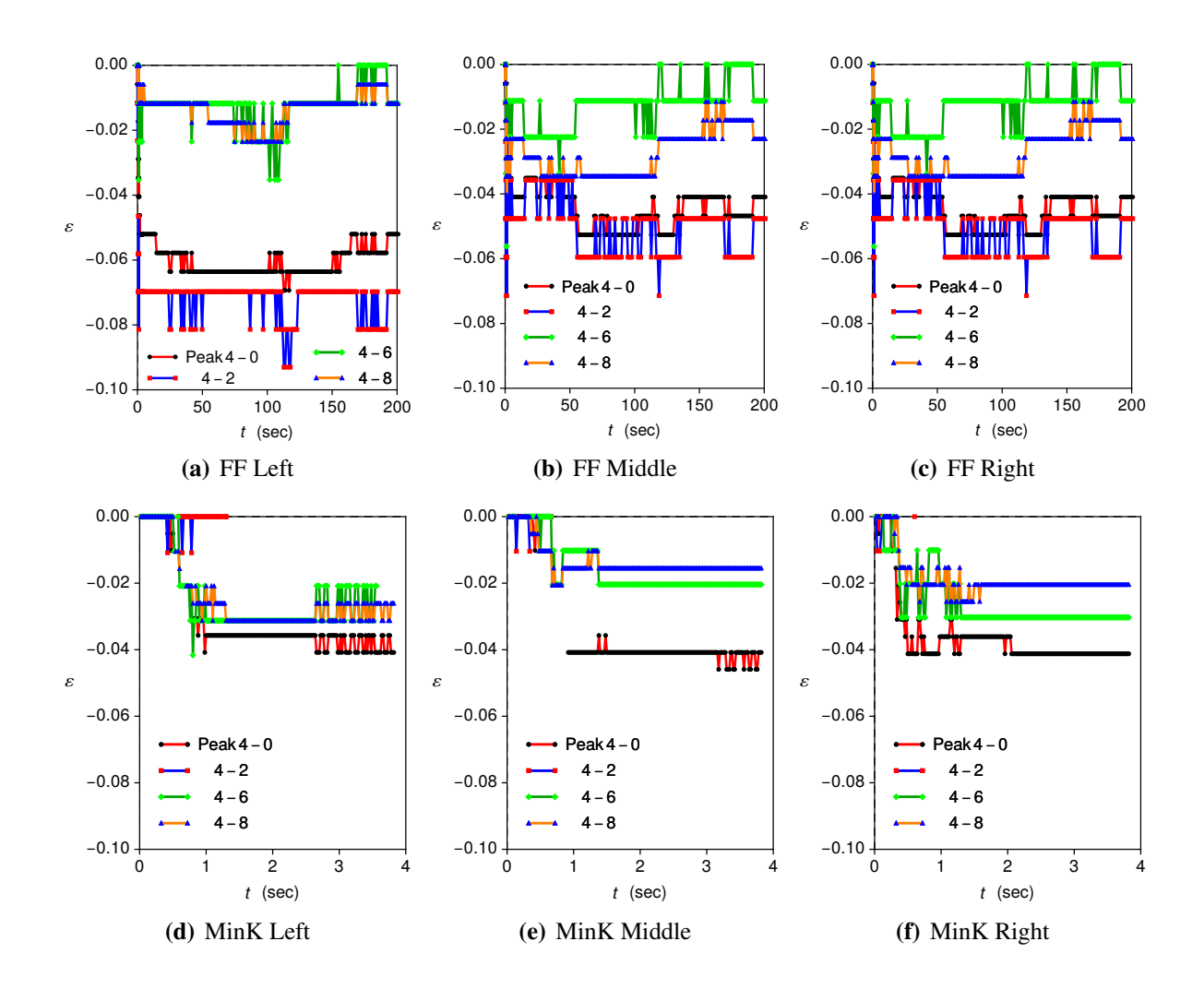


Figure 4.8. 10 cell stack strains. Strains in 10 Cell Fiberfrax Board and MinK insulated batteries averaged in the left, middle, and right image regions are shown. Strains are measured across peak image intensity regions as discussed in Figure 3.2. Because of smoke and other complications, frequently one cannot resolve intensity peaks throughout the entire tests. This loss of data is evident for the "FF Left" data. Characteristic strains are 6% in compression for FF and around 10% for MinK 3 cell batteries with the largest strains occurring in the right regions next to the heat paper.

Chapter 5

Conclusions

Key Findings

- 1. Stress relaxation during battery activation from the initially applied 210 psi was similar for the stacks using FF Board insulation layers. The nominal stack stress relaxed by approximately 90% for the 3, 5, and 10 cell stacks with FF Board. With MinK, stress relaxation during battery activation depends on the number of electrochemical cells. 3, 5, and 10 cell batteries relaxed by approximately 20%, 40%, and 60% compared with the nominally applied load. These results are found in Figure 4.2, and they reflect the very different compliance between the FF and MinK configurations in these tests—both to material and thickness of the insulation discs.
- 2. Displacements extracted from surface images differed between the FF Board and MinK batteries. The net stack strain for the FF batteries was fairly consistent regardless of the number of cells—approximately 3-5%. This observation is consistent with the observation that the FF batteries reached a common residual stress after activation for all configurations (see Figure 4.2). However, the strains were not uniform across the battery. Larger strains (up to 10%) were observed near the location where the heat paper contacted the stack, which is anticipated since these regions melt first. The 10 Cell FF Board experiment resulted in more uniform strains across the stack.
 - The MinK, by contrast, showed different total strains for the 3, 5, and 10 cell stacks of 10-15%, 5-10%, and 3-5% respectively. Also, the strains across the stack were more uniform for the MinK batteries than the FF batteries. The observation that average strains diminish with an increased ratio of total cell thickness to insulation thickness is sensible since, for a given displacement of the insulation layers associated with unloading, the strain in the battery stack decreases as the length absorbing this displacement increases.
- 3. Two displacement analysis methods were considered: the Peak tracking method and the FFT (Fast Fourier Transform) method. These methods were compared for the diameter-averaged net strain calculations and were in good agreement for the FF battery configurations, which validates both analysis techniques for producing accurate results. However, they did not agree well for the MinK configurations in general. The reasons behind this discrepancy are still under investigation. The FFT method does not suffer the pixelation noise problems seen by the Peak method. However, the Peak method proved to be somewhat more robust during

- the rise time analysis (where the flame front and smoke cause challenging image quality issues).
- 4. Force relaxation from 210 psi (initially applied) to 15-150 psi after ignition did not affect the measured electrochemical behavior of the batteries that were subjected to current density pulses of 82.2 mA cm⁻² above a nominal applied current density of 52.6 mA cm⁻². The square wave pulse was applied for 1 second with 15 seconds between pulses. During operation well before freeze-out, measured internal resistances were between 0.1 and 0.25 Ω and were not correlated to the residual force in the stacks. See Figure 4.4.
- 5. Control Experiments in which the electrochemical stack was not included (4 layers of insulation and heat pellets only but loaded to the same 210 psi) showed substantial mechanical force relaxation with the Fiberfrax Board insulation (75% load relaxation). However, the MinK insulation did not show an appreciable force relaxation during ignition (10% relaxation). Consequently, we can attribute all of the displacements observed in the MinK 3, 5, and 10 Cell stacks to the crush of the separator layers (and to a lesser extent the cathode layers).

Future Test Recommendations

- 1. Collector dimensions were not consistent during the 3, 5, 10 cell FF and MinK tests. In some cases, the small collector dimensions may have ultimately caused thermal runaway. We did not achieve a fully successful test matrix: 3, 5, 10 cell FF and MinK in at least duplicate for 12 tests total. Thicker collectors should be used for all tests to limit thermal runaway issues.
- 2. Temperature measurements were only made above the fixture and near the pancake load cell in a few cases to check the temperature history experienced by the load cell. The temperature never exceeded 15 °C above the starting temperature. Temperature measurements within the stack could improve the understanding of the electrochemical response of the cells.
- 3. Higher current pulses should be implemented for future tests. Though no correlation was found between the residual stack stress and the electrochemical resistance in this study, it is possible that this is because the tested current density was not high enough to cause this effect.
- 4. If displacement analysis remains important, we recommend:
 - (a) Take a tighter field of view image series zoomed in to improve resolution of the cells.
 - (b) Pursue and improve the FFT method for displacement analysis rather than the Peak method.
- 5. Consider a different battery tester setup that has a much faster data acquisition rate. The lower frequency of data acquisition from the Macor battery tester increased the complexity of the experimental setup and the analysis of the results.

References

- [1] John O'M. Bockris, Amulya K.N. Reddy, and Maria E. Gamboa-Aldeco. *Modern Electro-chemistry 2A*. Number DOI 10.1007/b113922 in Fundamentals of Electrodics. Springer US, 2 edition, 2000.
- [2] Ronald A. Guidotti and Patrick Masset. Thermally activated ("thermal") battery technology part I: An overview. *Journal of Power Sources*, 161:1443–1449, 2006.
- [3] Ronald A. Guidotti, Frederick W. Reinhardt, and Edward V. Thomas. Deformation study of separator pellets for thermal batteries. Sand report, Sandia National Laboratories, Sandia National Laboratories Albuquerque, New Mexico 87185-5800, 1995.
- [4] K. N. Long, P. L. Reu, E. C. Quintana, C. C. Roberts, E. D. Branson, D. K Wong, R. E. Fox, D. Ingersoll, and A. M. Grillet. Novel in situ experimental techniques to measure internal deformation, force, thermal behavior, and electrical performance of molten salt batteries. *Proceedings of the Power Sources Conference*, June 2014.
- [5] K. N. Long, C. C Roberts, S. A. Roberts, and A. M Grillet. The mechanics of pressed-pellet separators in molten salt batteries. Sand report unlimited release, Sandia National Laboratories, 2014.
- [6] K.N. Long, M.E. Stavig, C.C. Roberts, and L.A. Mondy. Mechanical behavior of mink and fiberfrax board insulation materials under battery packaging relevant conditions. MEMO (UUR) SAND2017-0370R, Sandia National Laboratories, 2017.
- [7] Hans-Georg Schweiger, Ossama Obeidi, Oliver Komesker, André Raschke, Michael Schiemann, Christian Zehner, Markus Gehnen, Michael Keller, and Peter Birke. Comparison of several methods for determining the internal resistance of lithium ion cells. *Sensors (Basel, Switzerland)*, 10(6):5604–5625, 2010.
- [8] Stephen Showalter and David Ingersoll. Private Communications Regarding Pressure in the Battery Stack During and After Thermal Battery Activation, August 2014.

DISTRIBUTION:

1	MS 0828	Tracie L. Durbin, 1512
1	MS 0828	Alex Headley, 1512
1	MS 0828	Philip L. Reu, 1512
1	MS 0346	Christine C. Roberts, 1512
1	MS 0346	Anne Grillet, 1513
1	MS 0836	Scott Roberts, 1513
1	MS 0613	David Ingersoll, 2500
1	MS 0613	Scott Ashbaugh, 2540
1	MS 0614	Kyle R. Fenton, 2545
1	MS 0614	Daniel E. Wesolowski, 2545
1	MS 0614	Hans Papenguth, 2547
1	MS 0614	Steven K. Showalter, 2547
1	MS 0613	Dennis K. Wong, 2548
1	MS 0613	Joseph E. Garni, 2548
1	MS 0840	Edmundo Corona, 1554
1	MS 0840	H. Eliot Fang, 1554
1	MS 0840	Kevin N. Long, 1554
1	MS 0840	Benjamin Reedlun, 1554
1	MS 0840	William M. Scherzinger, 1554
1	MS 0899	Technical Library, 9536 (electronic copy)

